Master's thesis

Master's thesis 2019 Bjørnar Gjesdal

**NTNU**
Norwegian University of
Science and Technology
Faculty of Natural Sciences
Department of Materials Science and Engineering

Bjørnar Gjesdal

# Investigation of a Non-Associated Flow Rule Incorporating Corner Effects and Comparison with an Elastoplastic Crystal Plasticity Model

June 2019

NTNU
Norwegian University of
Science and Technology

NTNU
Norwegian University of
Science and Technology

NTNU

Norwegian University of
Science and Technology

# Investigation of a Non-Associated Flow Rule Incorporating Corner Effects and Comparison with an Elastoplastic Crystal Plasticity Model

Bjørnar Gjesdal

Materials Science and Engineering
Submission date: June 2019
Supervisor: Bjørn Holmedal
Co-supervisor: Odd Sture Hopperstad

Norwegian University of Science and Technology
Department of Materials Science and Engineering

**Abstract**

The conventional associated flow rule, used in continuum plasticity models, is unsuited for precise prediction of necking in biaxially loaded sheets and plastic buckling [28], through bifurcation analysis. It is believed that the introduction of a corner on the subsequent yield surface of the material introduces the necessary destabilizing effect for a model to predict instabilities at realistic limit strains [32]. Several flow rules incorporating a corner effect have been introduced, with the latest being the one of Yoshida [36]. The proposed non-associated flow rule has been implemented in order to test the proposed constitutive model. In parallel, the rate-independent elastoplastic Taylor-Lin crystal plasticity model has been implemented, which does also incorporate the corner effects [16]. The two models have been compared by performing virtual strain path change experiments and comparing stress paths and the direction of the plastic deformation rate both with respect to the yield surface and the directions of the total deformation rate and the yield surface normal. The results indicate that the model qualitatively incorporates the corner effect, however, they also imply that calibration of the model to fit all types of experiments in a quantitative manner is not possible. To measure the difference between the two models an average angle between deviatoric stress points, has been used as the quantitative measure. An attempt has been made to find the optimal model parameters for the presented model, by minimizing the mentioned quantity. The overall conclusion is that the model incorporates the corner effect, however, the model might be unsuited if the speed at which it slides along the surface, is of great importance. It should be noted that the Taylor-Lin model is also an approximation, and how close its behavior is to reality, must be verified experimentally or by more advanced models, like CPFEM.

**Sammendrag**

Den konvensjonelle assosierte flyteregelen, brukt i kontinuums plastisitetsmodeller, er uegnet til prediksjon av flytinstabiliteter i tynne plater under biaksiell last og plastisk bukling [28] ved bifurkasjonsanalyse. Teorien tilsier at introduksjon av et hjørne på materialets instantane flyteflate tilfører en destabiliserende effekt, som er nødvendig for at en modell skal predikere instabiliteter, med bifurkasjonsanalyse ved realistiske tøyninger [32]. Flere flyteregler har blitt intodusert, som tar hensyn til hjørneeffekter, hvor det siste bidraget er foreslått av Yoshida i 2018 [36]. Den konstitutive modellen foreslått av Yoshida har blitt implementert for videre undersøkelser. Parallelt har en elastoplastisk rate-uavhengig krystallplastitisitetsmodell blitt implementert. Denne inkluderer også hjørneeffekten, og er derfor egnet til sammenlikning. De to modellene har blitt sammenliknet ved å utføre virtuelle tøyningsvei-endrings eksperimenter. Her har spenningsveien, retningen til den plastiske deformasjonsraten, vinkelen mellom den plastiske deformasjonraten og den totale deformasjonsraten og vinkelen mellom den plastiske deformasjonsraten og flyteflatenormalen blitt undersøkt. Resultatene indikerer at begge modeller kvalitativt introduserer en hjørneeffekt, men at det kvantitativt kan være utfordrende å finne modellparametere som gir overenstemmelse for alle typer eksperiment. For å måle den kvantitative avstanden mellom modellene har det blitt brukt en gjennomsnittlig vinkel mellom deviatoriske spenningspunkt. En optimeringsalgoritme har blitt implementert for å minimere dette målet, med gode resultater. Resultatene tyder likevel på at det trolig ikke er mulig å finne et sett med modellparameter som matcher alle eksperimenter, ettersom det ser ut til at sammenhengen for den krystallplastiske modellene er mer kompleks. Det er imidlertid ingen tvil om at den foreslåtte modellen kvalitativt implementerer hjørneeffekten.

# Acknowledgements

I would like to thank my supervisor, Bjørn Holmedal, for all help and guidance. His enthusiasm and interest in the topic have been a great inspiration. I would also like to thank my co-supervisors Odd Sture Hopperstad and Tomas Manik for providing helpfull knowledge and insight.

I have found working on the master thesis to be a fun and interesting study and I have learned a lot.

# Table of Contents

# 1 Introduction

Prediction of plastic instabilities and flow localization is important in all applications where metals are formed. In the automotive industry, simulations may replace several prototyping steps or be used to simulate car crashes, limiting the use of full-scale tests [7], and possibly greatly reducing both costs and time needed for the development of new products. The same argument may be made for a lot of other manufacturing processes where metal forming is involved. In order to perform such material simulations, a model of the material behavior is needed.

A continuum theory of plasticity aims to treat the material as a continuum with all the properties of a real plastic material. In reality, a metal is built up by atoms arranged in crystals and grains, which together make out the bulk material. Most materials are however used in a scale where the average properties are the most interesting, and what happens inside each grain at the atomic scale is of lesser interest. Hence a phenomenological plasticity model tries to account for the macroscopic behavior of the plastic material in a simple and computationally efficient manner.

The most common in a phenomenological plasticity model, is to use the associated flow rule and a smooth yield surface. Meaning that the direction of the plastic deformation rate is along the normal of a smooth yield surface. It has however been long known that this approach yields a model which is unsuited for prediction of plastic instabilities, like necking in biaxially loaded plates and buckling, as is pointed out by for instance Needleman and Tvergaard [28]. Marciniak and Kuczynski [27] proposed a workaround to the issues by introducing a finite imperfection in the material. This solution is widely used, although unrealistically large imperfections must be prescribed for the method to predict realistic limit strains, as is reported by Azrin and Backofen [3].

In 1949, Batdorf and Budiansky [6] introduced their slip theory of plasticity, using a yield surface with a sharp vertex to make the model predict realistic buckling loads. Since then it has been believed that the formation of a corner on the yield surface may introduce the necessary destabilizing effect for a model to be able to predict plastic

instabilities. Building on this idea, Stören and Rice [32] followed by Christoffersen and Hutchinson [8] introduced what is known as the $J_2$ deformation theory and $J_2$ corner theories, respectively. These deformation theories are known to be able to predict plastic instabilities at realistic strains and loads, but have not been generally adapted. The main criticism towards the $J_2$ deformation and corner theories is that they are path dependent and consequently computationally demanding if all loading modes should be considered, see Simo [31] or Kuroda and Tvergaard [22].

In an attempt to come up with a modified version of the widely accepted flow theory, which produce the same results as the $J_2$ deformation theories. Simo [31] proposed to modify the conventional flow rule, by allowing the direction of the plastic deformation rate to change, as if there were an instantaneous yield surface with a vertex inside the conventional yield surface. Otherwise, the model retains the conventional smooth yield surface. It is assumed that the plastic deformation rate, $\mathbf{D}^p$, is constrained to fall inside the cone spanned by the normals of the vertex facets. The introduction of such a vertex on the yield surface results in indeterminacy in the direction of $\mathbf{D}^p$, and consequently the model must present a method of determining this direction. Simo proposed that $\mathbf{D}^p$ should fall in the plane spanned by the normal of the yield surface and the deviatoric deformation rate, $\mathbf{D}'$. He further assumed that given $\mathbf{D}'$ is inside the vertex, $\mathbf{D}^p$ should be coaxial with $\mathbf{D}'$ and if $\mathbf{D}'$ is pointing out of the vertex, $\mathbf{D}^p$ should tilt equal to the half angle of the vertex, since it is constrained to lie inside the vertex. Since coaxiality between $\mathbf{D}^p$ and $\mathbf{D}'$ is assumed, an interesting feature of the model proposed by Simo, is that when $\mathbf{D}'$ is inside the vertex, the stress rate for a non-hardening material will be zero. Hence the stress point will not slide along the yield surface, but be stationary.

Kuroda and Tvergaard [21] further developed the model proposed by Simo. They formulated the model in a general form, introducing strain rate sensitivity, kinematic hardening and opening up the possibility to use an arbitrary yield surface. They also made an important modification to the flow rule, by relaxing the coaxiality between the plastic deformation rate and the deviatoric strain rate, demanded in Simo's model. The author thinks this is important, as it makes the model suitable even for non-hardening materials.

However the model proposed by Kuroda and Tvergaard was never implemented in three dimensions, only a plane stress model was explicitly formulated. While Simo aimed to mimic the behavior of the $J_2$ deformation theories, Kuroda and Tvergaard used crystal plasticity simulations to calibrate and test their model.

The latest non-associated flow rule is suggested by Yoshida [34] [36]. He has proposed a non-associated flow rule using the same decomposition as Simo, but a slight alteration of the way the model is presented. He also uses a different method of calibration, using the elastoplastic tangent modulus, as it is known that the formation of a vertex at the yield surface cause it to decrease. [35]. The model was first calibrated and tested using crystal plasticity simulations [34]. Later the model was tested against experiments on thin-walled tubes in tension and shear [36]. From the experiments, the model was slightly modified to fit the acquired data.

Experimental verification of the existence of a yield surface vertex has proved to be difficult. A review by Hecker [14] in 1976, reveals that up to that point the results had been contradicting. Measurement of the instantaneous yield surface is difficult since it is sensitive to the magnitude of the offset strain, which must be accurately decomposed into elastic and plastic parts. Additionally, the corner is blunted by viscous effects, as is shown by Pan and Rice [29], making the measurements even harder. Despite the challenges, more recent experiments by Kuwabara et al [23] seem to indicate that a vertex exists. Its existence has however been verified theoretically by Hill [16], for an elastoplastic rate-independent material, and by simulations by for instance Lin and Ito [25]. Hence it is known that the elastoplastic rate-independent Taylor-Lin crystal plasticity model incorporates a corner effect.

A crystal plasticity model is a model of the behavior of an aggregate of crystal grains. Each crystal grain may deform plastically by slip on the crystallographic slip planes and the aim of the model is to determine the amount of slip on each slip system in each crystal, and hence the plastic deformation, given a total deformation rate. The simplest of these theories is the Taylor type models [33], assuming that all grains are subject to the same aggregate strain, having the advantage that each grain may be treated independently. In

this study, the Taylor-Lin model [24] has been implemented, which is a generalization of Taylor's original model taking into account elasticity.

This study aims to investigate the non-associated flow rule presented by Yoshida, by comparison of virtual experiments calculated by an elastoplastic rate-independent crystal plasticity model, implemented in the authors project thesis. Some effort will be put on investigation of earlier work on the topic and the constitutive model proposed by Yoshida will be implemented. A framework for performing virtual experiments using the two models will be developed. A quantitative measurement of the deviation between the two models will be sought in order to perform calibration of the continuum model. Either way implementation of the novel constitutive model is nonetheless of interest as it, to the authors knowledge, has not been tested by other than Yoshida.

The models and all other code used in this study is freely available online at github to download following the link given in referecne [13]. It should be mentioned that the continumm models are named the constitutive models or phenemenological plasticity models througout the report. The crystal plasticity model might also be put in these categories, however it is only named crystal plasticity model in this study

# 2 Theory

## 2.1 Plastic instabilities

There are two generally applied approaches for the prediction of localization of plastic flow. Namely the imperfection approach and through bifurcation analysis. In the imperfection approach, a finite imperfection is introduced to the material of either geometrical or material character. The other, the bifurcation analysis is based on investigation of discontinuities in the equations given by the constitutive relation, leading to strain localization.

The simplest case of bifurcation analysis is for a circular tensile specimen. Where the first approximation for the limit strain is given by Considere's criterion, as the strain at which the true stress hardening rate equals the true stress [10]. For plates a criterion for localized necking is formulated by Hill [15], but its validity is constrained to strain ratios of $\epsilon_1/\epsilon_2 = \rho \leq 0$. Hence it is not valid for biaxially loaded plates where $\rho > 0$, as there, in this case, are no lines of zero extension. A framework for strain localization able to predict necking in the biaxial loading case, was introduced by Stören and Rice [32]. However, it was discovered that this criterion was sensitive to the constitutive formulation used and for instance, constitutive models using the associated flow rule and the conventional smooth yield surface, produce unrealistically high limit strains for the onset of necking in biaxially loaded plates [32].

To circumvent the bifurcation problem Marciniak and Kuczynski (M-K) [27] introduced a finite imperfection of material or geometric character, making it possible to predict the onset of necking using associated flow theory. An issue with the M-K theory is that an unrealistically deep groove needs to be prescribed in order to predict realistic limit strains, as is pointed out by for instance Azrin and Backofen [3]. Hence the groove thickness is in practice a calibration parameter, reducing the generality of the model.

## 2.2 Corner effects

The corner effects stem from the theory that the material develops a subsequent yield surface with a sharp vertex at the loading point. It follows that the corner effects is the physical implications of the formation of such a corner. The instantaneous yield surface with a sharp corner at the loading point and the conventional yield surface is illustrated in figure 2.1.

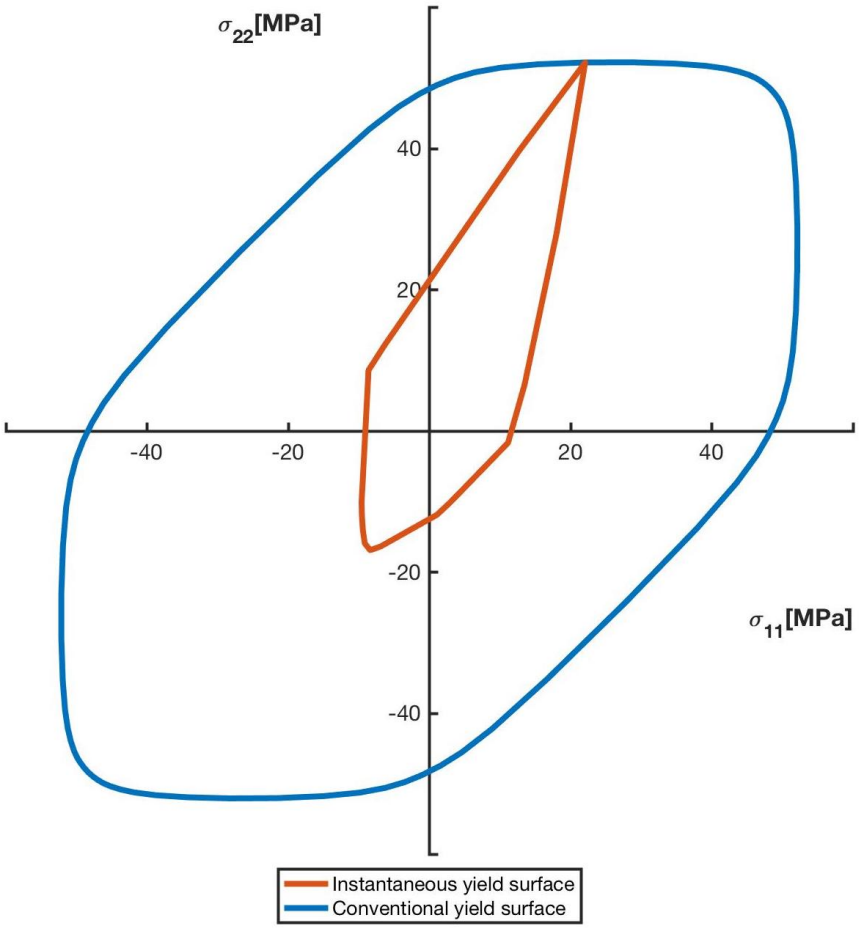


**Figure 2.1:** Illustration of the instantaneous subsequent yield surface together with the conventional yield surface.

Beyond the academic interest to determine if a corner is actually a phenomenon found in real metals, the implications of the corner effect for the prediction of plastic instabilities

are of great interest. It has been evident from the late 1940's that the classical flow theory, using a smooth yield surface and demanding normality of the plastic deformation rate, lead to unrealistically high limit strains for plastic instabilities [28] when bifurcation analysis is used. Especially for some loading modes, like buckling and bi-axially loaded plates, the predictions are unrealistic. The formation of a vertex on the yield surface relaxes the normality condition since there is no longer a well defined normal. The direction of the plastic strain rate consequently has increased freedom to accommodate any prescribed deformation. During a sudden change in stress or strain path, the material is hence able to more quickly, and at a lower energy barrier transition into the new loading mode. An example is for an equibiaxially loaded plate to form a neck, the loading mode must change from a biaxial state into plane strain. Due to the enhanced freedom of the plastic strain increment, the material is able to accommodate the new loading mode almost instantly. For a material following the associated flow rule the stress and strain must traverse the yield surface in order to reach plane strain, to the cost of a larger plastic work.

Incorporating the corner effects in a phenomenological plasticity model has shown to produce models capable of predicting buckling and necking loads at realistic levels, ever since it was proposed by Batdorf and Budiansky [6] in 1949. The same is valid for the $J_2$ deformation theory presented by Stören and Rice [32] and the $J_2$ corner theory introduced by Christoffersen and Hutchinson [8], which is known to predict these phenomena well [31]. These deformation theories have however not been generally adapted due to being too computationally demanding in comparison with the conventional flow theory.

Plastic flow rules incorporating the corner effects are able to predict plastic instabilities without the need for the introduction of finite imperfections. Predicting the onset of necking in bi-axially loaded plates, using bifurcation analysis, at a realisitc level is not possible using the conventional associated flow rule.

## 2.3 Yield surfaces

The yield surface is a surface in the stress space separating the elastic region from the plastic border. A stress point inside the yield locus corresponds to a material in an elastic deformation state. For a stress point lying on the yield surface, the material is deformed both plastically and elastically.

For a hardening material the yield surface expands with increasing plastic strains. It is important to notice that the stress can never be outside the yield surface. If a stress outside the current yield surface is to be reached the surface must expand, through hardening, to the point when the desired stress state is on the yield surface. During plastic deformation the stress point is always on the yield surface and moving with it. This is called the consistency condition.

In reality a metal is made of a large set of grains, each grain is a crystal, and each crystal has a set of slip systems. If a rate-independent material is assumed, the material will deform plastically when a critical resolved shear stress is reached on one of the slip systems, according to the Schmid hypothesis [10]. Each such slip system creates a set of paralell lines indicating the activation of the given slip system. The global material yield surface is hence the inner envelope off all such slip systems in the metal aggregate.

Most phenomenological models of plasticity are not concerned with calculating when a slip system is activated inside one of the material grains. It is only concerned with the global behaviour, and therefore a mathematical description of the yield surface is needed. The most renowned is the von Mises and Tresca yield surfaces. Both representing limiting cases of the class of isotropic yield surfaces described by the Hoshford/Hershey [17] yield surfaces. The expression for the yield surface is given by equation 2.1 below. Where $\sigma_1$, $\sigma_2$ and $\sigma_3$ are the prinicipal stresses.

$$\frac{1}{2}|\sigma_1 - \sigma_2|^n + \frac{1}{2}|\sigma_1 - \sigma_3|^n + \frac{1}{2}|\sigma_2 - \sigma_3|^n = \bar{\sigma}_{eq}^n \tag{2.1}$$

$$\begin{bmatrix} \sigma_{11} & \sigma_{12} & \sigma_{13} \\ \sigma_{21} & \sigma_{22} & \sigma_{23} \\ \sigma_{31} & \sigma_{32} & \sigma_{33} \end{bmatrix} = \mathbf{R} \begin{bmatrix} \sigma_1 & & \\ & \sigma_2 & \\ & & \sigma_3 \end{bmatrix} \mathbf{R}^{-1} \tag{2.2}$$

Due to the stress tensor being a real symmetric tensor, it is orthogonally diagonaizable [20], which means that it is possible to decompose the stress into a diagonal matrix and a rotational matrix, as in equation 2.2. Consequently there is always a change in coordinates, a rotation, where the shear components of the stress disappears. The resulting diagonal stress components are known as the principal stresses. For isotropic materials only the principal stresses are needed to determine the yield surface [19], as is evident from equation 2.1

The size of the yield surface is determined by an equivalent stress measure, $\bar{\sigma}_{eq}$, of the surface, which is a scalar function of all the components of the stress tensor. At least for most isotropic yield surfaces, the equivalent stress and strain correspond to the axial stress and strain in a uniaxial tensile test, which is applied for a practical calibration method, for the work hardening. The shape of the yield surface is determined by the exponent $n$. A Tresca yield surface corresponds to a power of $n = 1$ or $n = \infty$ and the von Mises yield surface to a power of $n = 2$ or $n = 4$. The reason each of the yield surfaces has two corresponding powers is that all surfaces may be found both in the range $[4, \infty]$ and $[1, 2]$. For fcc metals the power is found to be $n \approx 8.8$ and for bcc metals $n \approx 6$ by for instance Barlat [4].

In the case of a phenemenological model of plasticity it is desirable to represent the yield surface by all six stress components, as the gradient of the yield surface in the six-dimensional stress space is needed. Barlat [5] have analytically solved the eigenvalue problem of determining the principal stresses. This is used to formulate the Hoshford yield surface in the six dimensional stress space, which will be used in the constitutive model throughout this thesis. The gradient of the yield surface has also been calculated analytically, but due to the a rather lengthy calculation, both the yield surface and the gradient are given in appendix A.

It is also possible to define a yield surface for an anisotropic material. One such formulation is given in the same paper by Barlat [5]. In these cases more parameters are needed to calibrate the yield surface to the material, as there are less symmetries than in the isotropic case. Although the framework used throughout this project is able to cope with such a yield surface formulation, it has not been investigated. Yoshida [34] does however use an anisotropic yield surface for his constitutive model, like the one proposed by Barlat, since he is comparing results with anisotropic metals, with crystallographic textures.

## 2.4 Constitutive models for plasticity

In order to model the plastic behavior of metals, constitutive models mimicking what is observed in reality is needed. The common approach is to treat the material as a continuum. Which means the material is regarded as a continuous solid. Disregarding that the material in reality is made up of atoms ordered in grains of metal crystals. This makes sense since only the average macroscopic material behavior is of interest in most applications.

A flow theory of plasticity, which is a rate formulation, consists of three main constituents, a yield surface, a hardening rule, and a flow rule. The flow rule specifies how the plastic deformation rate is updated, hence it specifies the direction of the rate of plastic flow. The most common is the associated flow rule, stating that the plastic deformation rate is parallel to the gradient of the yield surface, or in other words, normal to the yield surface. Mathematically, this is given by equation 2.3, where $\mathbf{D}^p$ is the plastic deformation rate, $\dot{\lambda}$ a plastic consistency parameter and $\boldsymbol{\nabla} f$ is the gradient of the yield surface.

$$\mathbf{D}^p = \dot{\lambda} \boldsymbol{\nabla} f \tag{2.3}$$

A hardening rule is a rule determining the expansion of the yield surface as a function of the plastic strain. Usually, this is given by defining the equivalent stress as a function of an equivalent strain measure. Since a scalar strain measure is usually applied.

When a timestep is performed the flow rule determines the direction of plastic flow, and the plastic consistency parameter must be adjusted such that the step taken does not violate the consistency condition. The plastic deformation causes the yield surface to expand and consequently there must be a balance between the elastic and plastic deformation, such that the expansion of the yield surface is matched by the stress-rate given by the elastic deformation. This ensures that the stresspoint, during elastoplastic deformation is always on the yield surface.

The deformation theories mentioned in the introduction, are a type of phenomenological plasticity models which differs from the flow theories by that they are not rate formulated. They introduce a modulus, relating the total strain to the stress. This modulus must naturally be updated for each step. However, due to the irreversibility and path dependence of plastic deformation, caution is advised when using these models [19]. More detail is given in the section on deformation theories in the book "Continuum Theory of Plasticity" by Kahn [19].

## 2.5 Simo's model

The first to introduce a non-associated flow rule incorporating the corner effect was Simo [31]. He aimed to replicate the predictions of the $J_2$ deformation theories in a more computationally efficient manner. Simo proposed to use a conventional smooth yield surface, and modifies the flow rule to incorporate the flexibility implied by the formation of a vertex on the yield surface. In addition to the computational benefits, the formulation is based on the following observations:

1. **Physical implications of a vertex:**

   The formation of a vertex of semi-angle $\theta_{crit}$, as illustrated in figure 2.2, cause an indeterminacy in the plastic flow rule since the plastic deformation rate must lie within the hypercone formed by the vertex. Further the corner effect is not inherently dependent on a particular hardening law.

2. **Hypothesis:**

Loading paths tangential to a von Mises yield surface are purely elastic.

3. **The mutually excluding nature of the two above points:**

   For a vertex of semi-angle $\theta_{crit}$, elastic paths departing from the vertex form an angle $\frac{\pi}{2} + \theta_{crit}$ with the vertex axis, and not $\frac{\pi}{2}$, which is the angle of the tangential paths. This is illustrated in figure 2.2.

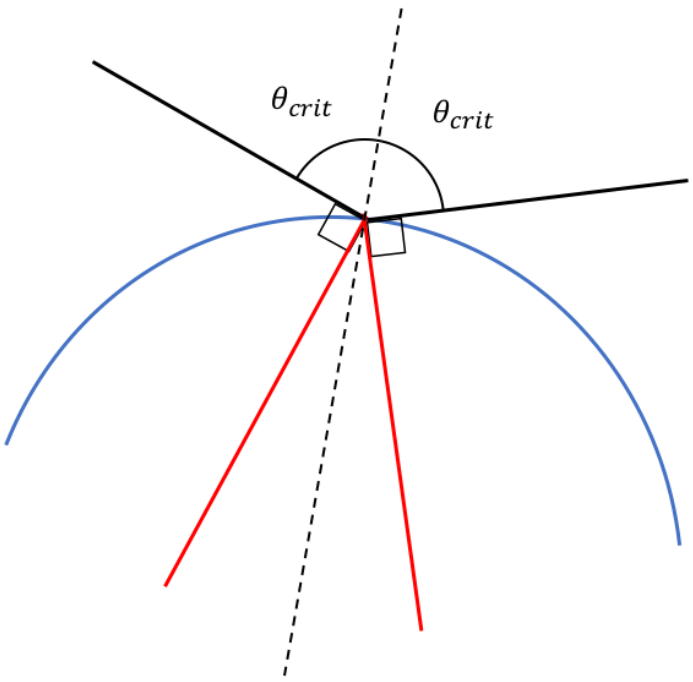


**Figure 2.2:** Illustration of the cone of semiangle $\theta_{crit}$ of permissible directions of $\mathbf{D}^p$ implied by the formation of a corner on the instantaneous yield surface. The outer yield surface is given in blue and the instantaneous yield surface in red.

The idea is hence that the plastic deformation rate, $\mathbf{D^p}$, lies in the plane spanned by the yield surface normal and the deviatoric deformation rate, $\mathbf{D}'$. It can therefore be decomposed into one component normal to the yield surface and one component along the projection of $\mathbf{D}'$ onto the tangential plane of the yield surface. $\mathbf{D^p}$ is further constrained to lie inside the cone of semi-angle $\theta_{crit}$.

The second assumption is necessary when the smooth conventional yield surface is to be used, otherwise it is clear that a deformation rate deviating more than $\frac{\pi}{2}$ radians from

the yield surface normal would yield release of plastic energy. Since plastic deformation is an irreversible process, the plastic energy must dissipate.

The model is based on an additive decomposition of $\mathbf{D}$ into an elastic and a plastic part, $\mathbf{D}^e$ and $\mathbf{D}^p$, as given by equation 2.4.

$$\mathbf{D} = \mathbf{D}^e + \mathbf{D}^p \tag{2.4}$$

Further, the objective Jaumann rate of Cauchy stress is given by equation 2.5. Where $\mathbf{D}^e$ is substituted using equation 2.4.

$$\mathring{\boldsymbol{\sigma}} = \mathscr{C}\left[\mathbf{D}^e\right] = \mathscr{C}\left[\mathbf{D} - \mathbf{D}^p\right] \tag{2.5}$$

The consistency condition is given according to equation 2.6, where $\bar{\sigma}$ is the von Mises equivalent stress and $g$ is the yield resistance as a function of the equivalent von Mises strain. The resistance to plastic flow may be determined from tensile test experiments or crystal plasticity simulations in uniaxial tension and fitted to a suitable mathematical expression, $g\left(\bar{\epsilon}^p\right)$.

$$f = \bar{\sigma}\left(\boldsymbol{\sigma}\right) - g\left(\bar{\epsilon}^p\right) \tag{2.6}$$

The von Mises equivalent stress is given according to equation 2.7, where $J_2$ is the second invariant of the Cauchy stress tensor. The energy conjugate von Mises equivalent strain is given by equation 2.8.

$$\bar{\sigma} = \sqrt{3J_2} \tag{2.7}$$

$$\dot{\bar{\epsilon}}^p = \sqrt{\frac{2}{3}\mathbf{D}_n^p : \mathbf{D}_n^p} = \dot{\lambda}\sqrt{\frac{2}{3}}||\mathbf{N}||$$
$$\bar{\epsilon}^p = \int_0^t \dot{\bar{\epsilon}}^p dt \tag{2.8}$$

The equations presented above, are all equal to the ones used in the conventional $J_2$ flow theory. The part distinguishing the model proposed by Simo from the conventional flow theory is the flow rule. The flow rule proposed is given by the set of equations 2.9, where $\mathbf{n}$ is the unit normal of the yield surface at the loading point, $\mathbf{m}$ is the normalized tangential component of the deviatoric deformation rate. The projection operator, $\mathbf{P}$, is projecting a tensor onto the tangential plane of the yield surface. $\dot{\lambda}$ is a plastic consistency parameter and $\hat{\delta}$ is a coefficient determining how much $\mathbf{D^p}$ is tilted. The decomposition of $\mathbf{D^p}$ is illustrated in figure 2.3.

$$\begin{aligned}
\mathbf{D^p} &= \mathbf{D}_n^p + \mathbf{D}_t^p = \dot{\lambda}\left[\mathbf{n} + \hat{\delta}\mathbf{m}\right] \\
\mathbf{n} &= \frac{\partial\bar{\sigma}}{\partial\boldsymbol{\sigma}} \Bigg/ \left|\frac{\partial\bar{\sigma}}{\partial\boldsymbol{\sigma}}\right| \\
\mathbf{P} &= \mathbf{I} - \mathbf{n}\otimes\mathbf{n} \\
\mathbf{m} &= \frac{\mathbf{P} : \mathbf{D}'}{||\mathbf{P} : \mathbf{D}'||}
\end{aligned} \tag{2.9}$$

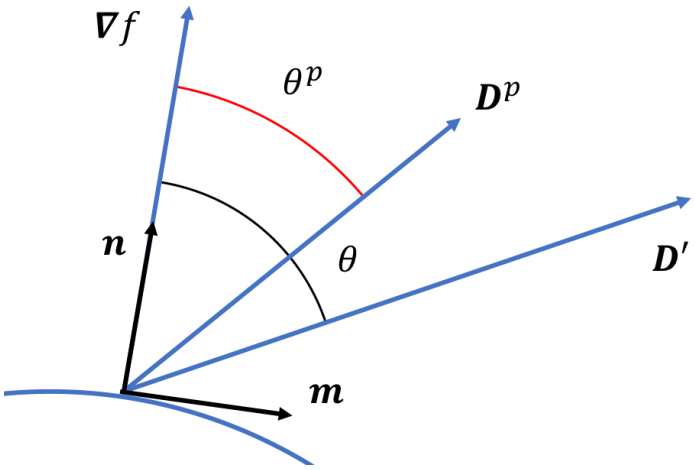


**Figure 2.3:** Illustration of how $\mathbf{D}^p$ is constructed from a component along the projection of $\mathbf{D}'$ onto the tangential plane of the yield surface, and a component in the normal direction of the yield surface. $\theta^p$ is the angle between the yield surface normal and $\mathbf{D}^p$ and $\theta$ is the angle between the normal and $\mathbf{D}'$.

The final piece needed for the model to be complete is $\hat{\delta}$, which is a parameter determining to what extent $\mathbf{D}^p$ is tilted.

**Simo's definition of $\hat{\delta}$**

Simo [31] defined the angle between the yield surface normal and the deviatoric deformation rate as $\theta$ according to equation 2.10. According to the first of the observations on which the model is based, the plastic deformation is restricted to lie within the hypercone of semiangle $\theta_{crit}$. Hence $\hat{\delta}$ is chosen such that the plastic strain rate is coaxial with the deformation rate deviator for cases when $\mathbf{D}'$ is inside the hypercone of the vertex. Meaning that $\theta^p = \theta$ in figure 2.2. For deformation directions outside the vertex, the angle is $\theta_{crit}$, as this is the maximum $\mathbf{D}^p$ is allowed to tilt.

$$cos\,(\theta) = \frac{\mathbf{n} : \mathbf{D}'}{||\mathbf{D}'||} \tag{2.10}$$

$$\hat{\delta} = \begin{cases} tan\,(\theta) & ,\theta \in [-\theta_{crit}, \theta_{crit}] \\ tan\,(\theta_{crit}) & ,|\theta| \in \left[\theta_{crit}, \frac{\pi}{2}\right] \end{cases} \tag{2.11}$$

This definition of $\hat{\delta}$ demands coaxiality between the deviatoric deformation rate and the plastic deformation rate. In the case of a non-hardening, perfect plastic material, when the plastic deformation rate is coaxial with the deviatoric deformation rate, it implies that there is no elastic deformation rate. When there is no elastic deformation rate, there can be no change in the stress state of the material, as is evident from equation 2.4. In the case of a hardening material, the plastic deformation expands the yield surface, making it necessary to deform the material elastically to ensure consistency at the end of the timestep, even if $\mathbf{D}'$ and $\mathbf{D}^p$ are coaxial.

## 2.6 Kuroda and Tvergaard's model

Simos model was modified by Kuroda and Tvergaard [21] to better fit the predictions of crystal plasticity simulations. Their model is formulated in a more general framework, taking into account strain rate sensitivity, kinematic hardening and permitting the use of an arbitrary yield surface. Although, the only explicit formulation presented, in their article [21], is for plane stress.

For the purpose of this study, kinematic hardening and strain rate sensitivity has been left out, and it follows that it is the alteration to the flow rule which is of the greatest interest. The formulation of the model is otherwise the same as the one by Simo, except that the yield surface may be chosen freely. In the plane stress formulation, Kuroda and Tvergaard have actually retained von Mises equivalent strain as the strain measure, despite not using the von Mises yield surface. Hence the equivalent stress and strain measure are not energy conjugated, in theri model.

The model [21] is then formulated according to equations 2.12 through 2.16 which are essentially the same as in Simo's model [31]. The only difference lies in the definition of $\hat{\delta}$ which is given by equation 2.17 below.

$$\mathbf{D} = \mathbf{D}^e + \mathbf{D}^p \tag{2.12}$$

$$\mathring{\boldsymbol{\sigma}} = \mathscr{C}\left[\mathbf{D}^e\right] = \mathscr{C}\left[\mathbf{D} - \mathbf{D}^p\right] \tag{2.13}$$

$$f = \bar{\sigma}\left(\boldsymbol{\sigma}\right) - g\left(\bar{\epsilon}^p\right) \tag{2.14}$$

$$\begin{aligned} \dot{\bar{\epsilon}}^p &= \sqrt{\frac{2}{3}\mathbf{D}_n^p : \mathbf{D}_n^p} = \dot{\lambda}\sqrt{\frac{2}{3}}||\mathbf{N}|| \\ \bar{\epsilon}^p &= \int_0^t \dot{\bar{\epsilon}}^p dt \end{aligned} \tag{2.15}$$

$$\begin{aligned} \mathbf{D^p} &= \mathbf{D}_n^p + \mathbf{D}_t^p = \dot{\lambda}\left[\mathbf{n} + \hat{\delta}\mathbf{m}\right] \\ \mathbf{n} &= \frac{\partial\bar{\sigma}}{\partial\boldsymbol{\sigma}} \Bigg/ \left|\frac{\partial\bar{\sigma}}{\partial\boldsymbol{\sigma}}\right| \\ \mathbf{P} &= \mathbf{I} - \mathbf{n}\otimes\mathbf{n} \\ \mathbf{m} &= \frac{\mathbf{P} : \mathbf{D}'}{||\mathbf{P} : \mathbf{D}'||} \end{aligned} \tag{2.16}$$

**Kuroda and Tvergaard definition of $\hat{\delta}$**

The modification of $\hat{\delta}$ is by the addition of a parameter $\alpha$ used to scale $\theta$. This introduces a new angle, $\theta^p$, between the yield surface normal and $\mathbf{D}^p$. Consequently it is relaxing the coaxiality between the strain rate deviator and the plastic deformation rate. The resulting definition of $\hat{\delta}$ is then as given in equation 2.17. By comparison with the model proposed by Simo, in section 2.5, it is evident that the only difference is the addition of the parameter $\alpha$. The parameter $\alpha$ is slightly less than unity, which prevents $\mathbf{D}^p$ from being fully coaxial with $\mathbf{D}'$. Hence the model will not be stationary for a non-hardening material, in contradiction to the model proposed by Simo [31].

$$\begin{aligned}
\alpha &= \frac{1}{c\,(g/G)+1} \\
\theta^P &= \begin{cases} \alpha\theta & ,\alpha\theta \in \left[-\theta^P_{crit}, \theta^P_{crit}\right] \\ \theta^P_{crit} & ,|\alpha\theta| \in \left[\theta^P_{crit}, \frac{\pi}{2}\right] \end{cases} \\
\hat{\delta} &= tan\left(\theta^P\right)
\end{aligned} \tag{2.17}$$

## 2.7 The constitutive model proposed by Yoshida

The consistutive model proposed by Yoshida is largely based upon Simo's original non-associated flow rule, at least in concept, but the detailed formulation is slightly different. The original model was presented in 2017 [34] with an update given in 2018 [36] with respect to acquired experimental results. The latest formulation is the model implemented in this study, hence a detailed elaboration of the models will be given.

The strain rate, $\mathbf{D}$, is additively decomposed into an elastic part $\mathbf{D^e}$ and a plastic part $\mathbf{D^p}$. The Jaumann rate of cauchy stress is further given by Hooke's law according to equation 2.18, where $\mathscr{C}^e$ is the elastic modulus given by Lame's constants, $\lambda$ and $G$, according to equation 2.19. $\delta_{ij}$ is the Kronecker delta.

$$\mathring{\boldsymbol{\sigma}} = \mathscr{C}^e\left[\mathbf{D}^e\right] = \mathscr{C}^e\left[\mathbf{D} - \mathbf{D}^p\right] \tag{2.18}$$

$$\mathscr{C}^e_{ijkl} = \lambda\delta_{ij}\delta_{kl} + G\left(\delta_{ik}\delta_{jl} + \delta_{il}\delta_{jk}\right) \tag{2.19}$$

The evolution of the critical equivalent stress, or yield strength, $g$, is given according to equation 2.20. $\sigma_0$ is the initial yield strength of the material, $\epsilon_0$ and $n$ is used as fitting parameters and $\bar{\epsilon}^p$ is the equivalent strain measure.

$$g\left(\bar{\epsilon}^p\right) = \sigma_0\Big(1 + \frac{\bar{\epsilon}^p}{\epsilon_0}\Big)^n \tag{2.20}$$

The yield surface used by Yoshida [34] is an anisotropic formulation adapted from Barlat [5]. However, for simplicity only the special case of an isotropic Hoshford/Hershey yield surface has been implemented, as described in section 2.3. Using the six component formulation of the yield surface is beneficial, since an analytic expression for the equivalent stress and the yield surface may be derived. If the formulation using principal stresses is used, an eigenvalue problem must be solved, and the gradient calculated numerically.

The consistency condition is then constructed from the two expressions for the equivalent stress, the yield stress as a function of equivalent strain and the equivalent stress from the yield surface. Hence the consistency equation is given by equation 2.21.

$$\bar{\sigma}\left(\boldsymbol{\sigma}\right) - g\left(\bar{\epsilon}^p\right) = 0 \tag{2.21}$$

The equivalent strain measure used is the von Mises strain, given in equation 2.22. This is the same as for the models proposed by Simo and Kuroda and Tvergaard, but as pointed out in the section on the Kuroda and Tvergaard model, the strain meassure is not energy conjugated when a different yield surface than the von Mises surface is used.

$$\begin{aligned} \dot{\bar{\epsilon}}^p &= \sqrt{\frac{2}{3}\mathbf{D}_n^p : \mathbf{D}_n^p} = \dot{\lambda}\sqrt{\frac{2}{3}}||\mathbf{N}|| \\ \bar{\epsilon}^p &= \int_0^t \dot{\bar{\epsilon}}^p dt \end{aligned} \tag{2.22}$$

$\mathbf{D}^p$ is given according to equation 2.23. The full tangential component of $\mathbf{D}'$ is used instead of the unit tangential direction, as is the case for Simo's model. The projection of the deviatoric strain rate, $\mathbf{D}'$, onto the tangential plane of the yield surface is calculated using the projection operator, $\mathbf{T}$, given in equation 2.24. $\mathbf{I}^{4s}$ is the fourth-order symmetric unit tensor, $\mathbf{I}$ is the second order unit tensor and $\mathbf{n}$ is the normalized yield surface normal. The tangential component of the deviatoric deformation rate is further found according to equation 2.25.

$$\mathbf{D}^p = \mathbf{D}^p_n + \mathbf{D}^p_t = \dot{\lambda}\mathbf{N} + \alpha \mathbf{D'}_t \tag{2.23}$$

$$\begin{aligned} \mathbf{T} &= \mathbf{I}^{4s} - \frac{1}{3}\mathbf{I} \otimes \mathbf{I} - \mathbf{n} \otimes \mathbf{n} \\ \mathbf{I}^{4s} &= \frac{1}{2}\left(\delta_{ik}\delta_{jl} + \delta_{il}\delta_{jk}\right) \end{aligned} \tag{2.24}$$

$$\mathbf{D'}_t = \mathbf{T} : \mathbf{D} \tag{2.25}$$

What determines how $\mathbf{D}^p$ tilts relative to $\mathbf{D'}$, is the parameters $\alpha$. In Yoshida's 2017 [34] formulation $\alpha$ is defined according to equation 2.26 below.

$$\alpha = \begin{cases} 1 - c_1\sqrt{\frac{g}{G}} - c_2\frac{\langle h \rangle}{G} & , \theta \in [0, \theta_{crit}] \\ \left(1 - c_1\sqrt{\frac{g}{G}} - c_2\frac{\langle h \rangle}{G}\right)\left(\frac{\pi/2-\theta}{\pi/2-\theta_{crit}}\right) & , \theta \in [\theta_{crit}, \pi/2] \\ 0 & , \theta \in [\pi/2, \pi] \end{cases} \tag{2.26}$$

In the latest paper by Yoshida [36], the original model was compared with experimental results which resulted in a minor update of the model. The model was updated for $\theta \in [\theta_{crit}, \pi/2]$ where the linear term is replaced. The updated model is given in equation 2.27.

$$\alpha = \begin{cases} 1 - c_1\sqrt{\frac{g}{G}} - c_2\frac{\langle h \rangle}{G} & , \theta \in [0, \theta_{crit}] \\ \left(1 - c_1\sqrt{\frac{g}{G}} - c_2\frac{\langle h \rangle}{G}\right)\frac{\tan(c_3(\theta-\theta_{crit})+\theta_{crit})}{\tan(\theta)} & , \theta \in [\theta_{crit}, \pi/2] \\ 0 & , \theta \in [\pi/2, \pi] \end{cases} \tag{2.27}$$

The unloading criterion for the model is given by equation 2.28, implying that $\dot{\lambda}$ and $\alpha$ should be set to zero in these cases. The criteria gives $\theta \leq \pi/2$ which in equations 2.26 and 2.27 yields $\alpha = 0$.

$$\mathbf{N} : \mathbf{D'} \leq 0 \tag{2.28}$$

Yoshida proposes to use an explicit time integration scheme for the model, based upon calculating an elastoplastic modulus. The plastic consistency parameter $\dot{\lambda}$ is derived through taking the derivative of the consistency condition, equation 2.21. The expression is given in equation 2.29, where $\mathbf{N}$ is the yield surface gradient, $\mathscr{C}^e$ is the elastic modulus and $h$ is hardening rate, $h = \frac{dg}{d\bar{\epsilon}^p}$.

$$\dot{\lambda} = \frac{\mathbf{N} : \mathscr{C}^e : \mathbf{D}}{\mathbf{N} : \mathscr{C}^e : \mathbf{N} + \sqrt{\frac{2}{3}}||\mathbf{N}||h} \tag{2.29}$$

Using the derived $\dot{\lambda}$ together with equation 2.23, $\mathbf{D}^p$ in equation 2.18 may be substituted and $\mathbf{D}$ factored out, arriving at the the elastoplastic modulus $\mathscr{C}^{ep}$ as given in equation 2.30. For more details the reader is referred to the original paper by Yoshida [34].

$$\mathscr{C}^{ep} = \mathscr{C}^e - \frac{\mathscr{C}^e : \mathbf{N} \otimes \mathbf{N} : \mathscr{C}^e}{\mathbf{N} : \mathscr{C}^e : \mathbf{N} + \sqrt{\frac{2}{3}}||\mathbf{N}||h} - \alpha\mathscr{C}^e : \mathbf{T} \tag{2.30}$$

Finally the stress rate is given by equation 2.31:

$$\mathring{\boldsymbol{\sigma}} = \mathscr{C}^{ep} : \mathbf{D} \tag{2.31}$$

This stress update scheme is however not the one used for the simulations conducted in this paper. To better ensure consistency throughout the experiment, an implicit algorithm has been implemented instead.

## 2.8 Model calibration

**Vertex angle $\theta_{\text{crit}}$**

The only fitting parameter shared between the proposed non-normality models is the critical angle of the yield surface vertex, determining to what extent $\mathbf{D}^p$ is allowed to tilt.

Simo provides no method of calibration of the critical angle, but do simulations for a range of critical angles between $\theta_{crit} = 0$ and $\theta_{crit} = \pi/2$. However the focus seems to be qualitative verification of the model, rather than quantitative calibration. It is however

pointed out that the model degenerates to the conventional associated flow rule when $\theta_{crit} = 0$.

Kuroda and Tvergaard calibrated their model using crystal plasticity simulations. The specific procedure used to calibrate $\theta_{crit}$ is not provided, but it is outlined that the angle is determined by performing a large strain path change. The strain path change must be large enough that $\mathbf{D}'$ tilts outside the vertex for some part of the experiment. The critical angle may then be read off as the threshold angle, which is the maximum observed tilt angle. If it is assumed that $\mathbf{D}^p$ is constricted to lie inside the cone formed by the vertex, $\mathbf{D}^p$ will take the critical angle relative to the gradient for some time following a large abrupt strain path change. It was found that the value of $\theta^p$ did not vary greatly during the early stages of the strain path change, this behavior was found to be close to independent of the prestrain level. The simulations indicated an angle of approximately $\theta^p = 20°$.

Yoshida, in the 2017 version of the model, does not have a quantitative way of determining the appropriate $\theta_{crit}$. Simulations are performed for a range of angles, and the range from 0 to 10° is determined as the range for which the best fits were found. The relation between $\theta$ and $\theta^p$ is used for comparison, which is the angle between $\mathbf{N}$ and $\mathbf{D}'$ and $\mathbf{N}$ and $\mathbf{D}^p$ respectively, just after the strain path change. The crystal plasticity simulations performed by Yoshida show a linear relationship between $\theta$ and $\theta^p$, for the initial tilt, up to about 30°. In this region, the crystal plasticity model and the constitutive model are found to be in good agreement. The $\theta$ - $\theta^p$ relation for the constitutive model is parabolic, whereas the crystal plasticity model is closer to linear, hence it is difficult to determine which $\theta_{crit}$ gives the best results.

The alteration done in the 2018 version of Yoshida's model is to make the model fit the experimental $\theta$ - $\theta^p$ to a greater extent. Hence a more linear relationship, with a kink, is proposed. It appears that the model is calibrated such that the $\theta$ - $\theta^p$ relations gives a good fit, however, no information regarding the method is given.

Kuroda and Tvergaard are the only ones presenting a quantitative way of determining

the critical angle of the vertex. It should be pointed out that for the models proposed by Simo and Kuroda and Tvergaard, setting $\theta_{crit} = 0$ makes the models degenerate to the associated flow rule. This is however not the case for the models proposed by Yoshida.

**Kuroda and Tvergaards model**

Other than $\theta_{crit}$ there is only one parameter which must be calibrated in the flow rule, eq. 2.16 , which is $c$. To fit $c$, the ratio between the $\theta^p$ and $\theta$ is used as an approximation of $\alpha$. Hence the parameter $c$ may be determined by correlating the variation in $\alpha$ to the variation in yield strength. It is found that even though the parameter is not in reality a constant, it is treated as one, in order to maintain model simplicity.

The model by Kuroda and Tvergaard does also use the yield surface exponent as a calibration parameter, for their plane stress specific formulation. The crystal plasticity simulations permit the stress path to pass inside the outer conventional yield surface. This behavior is naturally not compatible with a flow rule following the outer yield surface, as it would lead to plastic unloading. Hence increasing the yield surface exponent, bringing it closer to the Tresca surface, might give the model increased explanatory power when deviations from equibiaxial load are performed. This is because the edges of the surface are straightened. However, the higher exponent yield surface still passes through the same points in equibiaxial and uniaxial load. A possible negative issue is that the model would produce more error in conventional proportional load, as the shape of the yield surface is altered.

**Yoshida's models** In the initial model proposed by Yoshida, there are two fitting parameters, $c_1$ and $c_2$, besides the critical angle, which are calibrated the same way for both models. The parameters are calibrated using the elastoplastic tangent modulus. It can be shown that for an isotropic material in uniaxial tension the normalized shear modulus $\frac{\mathscr{C}^{ep}}{G}$ equals $1-\alpha$. Since $c_1$ is the coefficient of $\sqrt{\frac{g}{G}}$ and $c_2$ the proportionality constants of $\frac{\langle h \rangle}{G}$, $c_1$ may be fitted by performing simulations of non-hardening materials with different critical yield stresses, hence $g$ is varied. The parameter $c_2$ may subsequently be fitted by crystal plasticity simulations of different linearly hardening materials. The parameter $c_1$ is found to be 0.3 and the parameter $c_2 = 0.5$ by Yoshida [34].

It is worth noting that in order to calibrate the model, it is necessary to compute the elastoplastic modulus from the crystal plasticity model. The elastoplastic modulus is, as in the case for Yoshida's constitutive model, a modulus which is multiplied by the total deformation gradient to yield the stress rate. This is a rather complicated expression, and an exercise in operations on fourth order tensors to derive, which would otherwise not be needed. Hence it may be regarded as a slight drawback of the model, as it adds complexity.

For Yoshida's 2018 model [36] there is introduced another fitting parameter $c_3$ which is used to determine the slope of $\theta^p$ vs $\theta$, and fits in the updated expression for $\theta$ in the range from $\theta_{crit}$ to $\frac{\pi}{2}$. No information on how this parameter is fitted is given. It appears to be fitted such that the $\theta^p$ - $\theta$ relation of the model matches that found from the experiments.

## 2.9 Crystal plasticity

A poly-crystal plasticity model tries to model how a material made out of an aggregate of grains behaves under deformation. Throughout the 1920 and 1930s, much research on single crystals was conducted. However, generalizing the knowledge of how single crystals deformed to a poly-crystalline aggregate brought two challenges. First, it was evident that no voids were formed in the material during deformation. Secondly, the stress should be balanced between the grains.

Sachs [30] proposed a model assuming the same stress in all grains. Such a model would ensure that the material was in a balanced stress state, however the differently oriented grains would deform differently, and cause incompatibility at the grain boundaries, meaning that voids would form.

The opposite assumption was made by Taylor [33]. He proposed that all grains are subjected to the same deformation. Such a formulation would ensure compatibility between the grains, at the sacrifice of internal stress balance. Taylor argued that no voids were observed during tensile tests. He further assumed that each grain could be treated independently. As a result, the problem amounts to solving a deformation problem for a

single crystal. The aggregate variables are consequently the average over all grains.

An fcc material has 12 slip systems. Taylor showed that for such a crystal to accommodate any deformation, only five slip systems are needed. Hence the problem of determining the correct set of 5, out of the 12 slip systems, arise. Taylor further assumed that the set corresponding to the minimum virtual work should be used. This reduces the potential set of slip systems drastically, however the problem is not solved, as it is possible to show that there is more than one solution corresponding to minimum virtual work. As a consequence, it is ambiguous which set of slip systems should be selected. This ambiguity is known as the Taylor-ambiguity. A review of the Taylor ambiguity is given by for instance Manik et al. [26].

The crystal plasticity model used in this study is an elastoplastic rate-independent Taylor-type model. In the original model proposed by Taylor, the elastic strain was neglected, as it may be seen as negligible compared to the plastic, hence it is a rigid-plastic model. A crystal plasticity formulation taking into account elasticity was first formulated by Lin [24]. The elastoplastic generalization of Taylor's original model is therefore known as the Taylor-Lin model. In this work, the Taylor-Lin model has been implemented following the algorithm proposed by Anand and Kothari [1].

The main criticism towards the Taylor type crystal plasticity models is that it does not satisfy stress equilibrium across the grain boundaries. On the contrary this is also the benefit of the model, as each grain may be treated independently, easing the calculations. In an attempt to solve this issue several self-consistent models have been proposed. The basic idea is to treat each grain as an inclusion in a continuous media, having properties similar to the average of the aggregate, and ensure that there is equilibrium between the grain and the surrounding continuum. For further details, the reader is referred to chapters 11 and 12 of the book "Continuum Theory of Plasticity" by Khan [19].

## 2.10 Crystal plasticity model

The implementation of the Taylor Lin model used is in large parts adapted from Anand and Kothari [1]. There are some elements of the derivation which are inspired by a paper by Dumolin [11], who has derived a similar algorithm and displays more thoroughly some of the steps of the derivation. The section below is largely copied from the authors project thesis for completeness, as the project thesis is not publicly available.

Throughout the derivation all tensors are expressed in the initial lattice frame, unless specified otherwise. The tensors are denoted according to the convention used in continuum mechanics and the reader is referenced to the book "Continuum Theory of Plasticity" by Khan [19] for further explanation.

For the time integration scheme values at current time are denoted $t$ and after one time step $\tau = t + \Delta t$. The initially given parameters are listed in the list below.

- Deformation gradient at both times, $\mathbf{F}(t)$ and $\mathbf{F}(\tau)$.
- Orientation of the the slip systems

$$(\mathbf{m_0^\alpha}, \mathbf{n_0^\alpha})$$

  Where $\mathbf{m_0^\alpha}$ is the slip direction and $\mathbf{n_0^\alpha}$ is the slip plane normal. The subscript 0 indicate that the directions are in the initial lattice orientation. Worth noting is that these directions are time independent, as will be shown in the derivation below.

- Initial Cauchy stress, $\mathbf{T}(t)$
- Initial plastic deformation gradient, $\mathbf{F^P}(t)$
- The Critical resolved shear stress, $s^\alpha(t)$

In order to advance one time step one must calculate, $\mathbf{F^P}(\tau)$, $\mathbf{T}(\tau)$ and $s^\alpha(\tau)$.

First it should be established that the deformation gradient is decomposed multiplicatively into an elastic and a plastic part, according to equation 2.32. The concept is also illustrated in figure 2.4. The plastic deformation gradient describes deformation of the

material by plastic slip. The lattice rotation and elastic deformation is incorporated into the elastic deformation gradient, $\mathbf{F^e}$.

$$\mathbf{F}(\tau) = \mathbf{F^e}(\tau)\,\mathbf{F^p}(\tau) \tag{2.32}$$

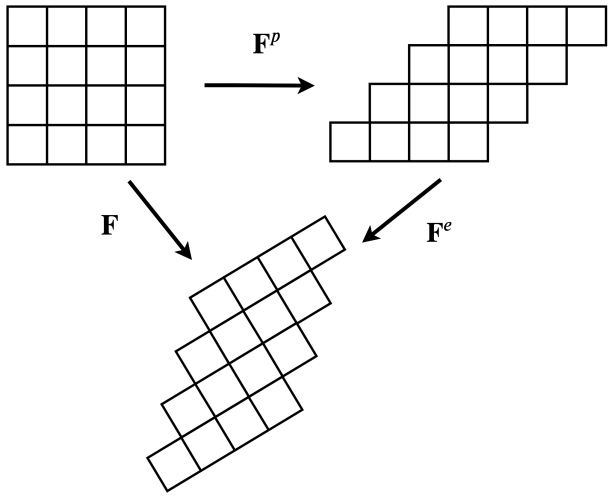


**Figure 2.4:** Multiplicative decomposition of the deformation gradient into a plastic and an elastic component. The lattice rotation is incorporated into the elastic deformation gradient.

As is mentioned, the lattice rotation is included in $\mathbf{F^e}$, and for infinitesimal elastic deformations the stretch component can be neglected. Both the polar decomposition and the approximation of $\mathbf{F^e}$ as a rotation matrix, shown in equation 2.33, will be used later in the derivation.

$$\mathbf{F^e} = \mathbf{RU} \approx \mathbf{R} \tag{2.33}$$

The stress in the initial configuration can be calculated according to Hooke's law as

$$\mathbf{T}^*(\tau) = \mathscr{C}\left[\mathbf{E^e}(\tau)\right] \tag{2.34}$$

Where $\mathbf{E^e}(\tau)$ is an elastic strain measure given by the right Cauchy-Green tensor as

$$\mathbf{E^e}(\tau) = \frac{1}{2}\left(\mathbf{C^e}(\tau) - \mathbf{I}\right) \tag{2.35}$$

The Right Cauchy-Green tensor is given by

$$\mathbf{C^e}\left(\tau\right) = \left(\mathbf{F^e}\left(\tau\right)\right)^{\mathbf{T}} \mathbf{F^e}\left(\tau\right) \tag{2.36}$$

The stress $\mathbf{T}^*\left(\tau\right)$ is the Second Piola-Kirchoff stress, and can be regarded as the engineering stress. It is an energy conjugate to the strain meassure $\mathbf{E^e}\left(\tau\right)$. The Cauchy stress, $\mathbf{T}\left(\tau\right)$ is related to the second Piola-Kirchoff stress, $\mathbf{T}^*\left(\tau\right)$, through the following relation.

$$\mathbf{T}^*\left(\tau\right) = \mathbf{F^e}\left(\tau\right)^{-1} \left\{det\left(\mathbf{F^e}\left(\tau\right)\right) \mathbf{T}\left(\tau\right)\right\} \mathbf{F^e}\left(\tau\right)^{-T} \tag{2.37}$$

The Kirchoff stress, $\mathbf{\Gamma}\left(\tau\right)$, is then defined as

$$\mathbf{\Gamma}\left(\tau\right) = \mathbf{det}\left(\mathbf{F^e}\left(\tau\right)\right) \mathbf{T}\left(\tau\right) = \mathbf{F^e}\left(\tau\right) \mathbf{T}^*\left(\tau\right) \mathbf{F^e}\left(\tau\right)^T \tag{2.38}$$

Further the critical resolved shear stress on each slip system can be determined from the following equation, equation 2.39. Where $\mathbf{n}^\alpha$ and $\mathbf{m}^\alpha$ are the slip plane and slip direction vector in the current, deformed, configuration. These are related to the directions in the initial crystal configuration through equation 2.40

$$\tau^\alpha\left(\tau\right) = \mathbf{m}^\alpha \cdot \mathbf{\Gamma}\left(\tau\right) \mathbf{n}^\alpha \tag{2.39}$$

$$\begin{aligned} \mathbf{n}^\alpha &= \mathbf{n}_0^\alpha \mathbf{F^e}^{-1} \\ \mathbf{m}^\alpha &= \mathbf{F^e} \mathbf{m}_0^\alpha \end{aligned} \tag{2.40}$$

The term $\mathbf{\Gamma}\left(\tau\right) \mathbf{n}^\alpha$ in equation 2.39 is the traction on the slip plane, or the force per area. The critical resolved shear stress is then given as the component of the traction in the direction of the slip plane, hence $\tau^\alpha\left(\tau\right)$ is the projection of the traction onto the slip direction. By substituting equation 2.38 into equation 2.39 equation 2.41 is formed.

$$\tau^{\alpha}(\tau) = \{\mathbf{C^e}(\tau)\,\mathbf{T}^*(\tau)\} : \mathbf{S_0^\alpha} \tag{2.41}$$

$$\mathbf{S_0^\alpha} = \mathbf{m_0^\alpha} \otimes \mathbf{n_0^\alpha} \tag{2.42}$$

The dot product, or inner product of two matrices $\mathbf{S}$ and $\mathbf{T}$ is defined as:

$$\mathbf{S} : \mathbf{T} = trace\left(\mathbf{S^T T}\right) \tag{2.43}$$

And the tensor product of two vectors $\mathbf{n}$ and $\mathbf{m}$ is defined to be:

$$\mathbf{n} \otimes \mathbf{m} = \begin{bmatrix} n_1 m_1 & n_1 m_2 & n_1 m_3 \\ n_2 m_1 & n_2 m_2 & n_2 m_3 \\ n_3 m_1 & n_3 m_2 & n_3 m_3 \end{bmatrix} \tag{2.44}$$

For infinitesimal elastic strains the Right Cauchy-Green deformation tensor may be neglected and the stress is given by equation 2.46. If $\mathbf{F^e}$ was purely a rotation matrix, the Right Cauchy-Green deformation tensor would become the identity matrix, due to the orthogonality of the rotation matrix, as shown in equation 2.45.

$$\mathbf{C^e} = \mathbf{F^{eT} F^e} \approx \mathbf{R^T R} = \mathbf{I} \tag{2.45}$$

$$\tau^{\alpha}(\tau) = \mathbf{T}^*(\tau) : \mathbf{S_0^\alpha} \tag{2.46}$$

Each slip system can either be active or inactive. If a slip system is inactive the critical resolved shear stress must be less than critical. For an active slip system the criterion is that the shear stress on the system is equal to the critical shear stress. If this criterion is satisfied, it is said that consistency is maintained. Naturally if the shear stress on a system is at the critical value, the slip system would slip until equilibrium is achieved. Mathematically the consistency condition, for the active slip systems, is given by equation 2.47.

$$|\tau^{\alpha}(\tau)| = s^{\alpha}(\tau) \tag{2.47}$$

The integration algorithm is based on solving the above equation, at the end of the time-step, by using an elastic predictor. This means to preliminary assume that the deformation step is purely elastic. Unless the material is in the elastic region, this assumption results in resolved shear stresses which exceed the critical shear stress on some of the slip systems, which in turn are categorized as potentially active, $\mathscr{PA}$. The goal of the algorithm is then to do a reverse map of the resolved shear stress in order to achieve consistency on the set of potentially active slip systems. In practice this means to express the plastic deformation gradient by the slip increments, according to equation 2.48, and then calculate the magnitude of the slip increments needed in order to ensure consistency at the end of the timestep.

$$\mathbf{F^p}(\tau) = \left\{\mathbf{I} - \sum_{\alpha \in \mathscr{PA}} sgn\left(\tau^{\alpha}(\tau)\right) \Delta\gamma^{\alpha} \mathbf{S_0^{\alpha}}\right\} \mathbf{F^p}(t) \tag{2.48}$$

Worth noting is that equation 2.48 is a forward euler integration of the plastic deformation gradient using the plastic velocity gradient. According to the following set of equations, 2.49.

$$\begin{aligned}
\dot{\mathbf{F}}^{\mathbf{p}}(\mathbf{t}) &= \mathbf{L}_{\mathbf{0}}^{\mathbf{p}}(\tau)\, \mathbf{F}^{\mathbf{p}}(\mathbf{t}) \\
\mathbf{F}^{\mathbf{p}}(\tau) &= \mathbf{F}^{\mathbf{p}}(\mathbf{t}) + \mathbf{L}_{\mathbf{0}}^{\mathbf{p}}(\mathbf{t})\, \mathbf{F}^{\mathbf{p}}(\mathbf{t}) \Delta t \\
\mathbf{F}^{\mathbf{p}}(\tau) &= \left\{\mathbf{I} + \mathbf{L}_{\mathbf{0}}^{\mathbf{p}}(\mathbf{t}) \Delta t\right\} \mathbf{F}^{\mathbf{p}}(\mathbf{t}) \\
\mathbf{L}_{\mathbf{0}}^{\mathbf{p}}(\mathbf{t}) \Delta t &= \sum_{\alpha \in \mathscr{A}} sgn\left(\tau^{\alpha}(\tau)\right) \dot{\gamma}^{\alpha} \Delta t \mathbf{S_0^{\alpha}} \\
\Delta\gamma^{\alpha} &= \dot{\gamma}^{\alpha} \Delta t
\end{aligned} \tag{2.49}$$

As mentioned the first step of the algorithm is to define the trial elastic stress, by assuming the plastic deformation gradient does not change during the deformation step, according to equation 2.50

$$\mathbf{F^e}\left(\tau\right)^{\mathbf{tr}} = \mathbf{F}\left(\tau\right)\mathbf{F^{-p}}\left(\mathbf{t}\right) \tag{2.50}$$

By applying equations 2.36,2.35, 2.34 and 2.46 one can calculate a trial resolved shear stress:

$$\tau^{\alpha}\left(\tau\right)^{tr} = \mathbf{T}^{*}\left(\tau\right)^{tr} \cdot \mathbf{S_0^{\alpha}} \tag{2.51}$$

The systems loaded above the critical yield stress is then denoted as potentially active, and the ones below as inactive.

$$\begin{aligned} |\tau^{\alpha}\left(\tau\right)^{tr}| < s^{\alpha}\left(t\right) &\Rightarrow \notin \mathscr{PA} \\ |\tau^{\alpha}\left(\tau\right)^{tr}| \geq s^{\alpha}\left(t\right) &\Rightarrow \in \mathscr{PA} \end{aligned} \tag{2.52}$$

Not all systems in the set of potentially active is necessarily activated, and the set of systems with slip activity when moving on from the time step are denoted $\mathscr{A}$ and is a subset of $\mathscr{PA}$

The primary use of the trial elastic shear stress is to determine the set $\mathscr{PA}$, it can further be shown that the actual resolved shear stress at time $\tau$ is given by the reverse map given by equation 2.53, in which the plastic deformation gradient given in equation 2.48 is used to calculate the elastic deformation gradient. The reverse map is however not inherently linear in $\Delta\gamma^{\alpha}$, and in order to end up with a linear equation, higher order terms of $\Delta\gamma^{\alpha}$ are neglected. Worth noting is that this is all done under the assumption that the sign of the final resolved shear stress of a slip system is equal to the sign of the trial resolved shear stress.

$$|\tau^{\alpha}\left(\tau\right)| = |\tau^{\alpha}\left(\tau\right)^{tr}| - \sum_{\beta\in\mathscr{A}} \left\{ sgn\left(\tau^{\alpha}\left(\tau\right)^{tr}\right) sgn\left(\tau^{\beta}\left(\tau\right)^{tr}\right) \mathbf{S_0^{\alpha}} : \mathscr{C}\left[sym\left(\mathbf{C^e}\left(\tau\right)^{tr}\mathbf{S_0^{\beta}}\right)\right]\right\} \Delta\gamma^{\beta} \tag{2.53}$$

The last piece needed to build the linear set of equations for the consistency condition is the hardening of the slip systems. The critical resolved shear stress is changing with slip activity on the actual system, and on other systems. The hardening of a system due to other systems is known as latent hardening. A model for the hardening of the slip systems is taken from Anand and Kothari [1], and is given in equation 2.54.

$$s^{\alpha}(\tau) = s^{\alpha}(t) + \sum_{\beta \in \mathscr{A}} h^{\alpha\beta}(t)\,\Delta\gamma^{\beta} \tag{2.54}$$

$$\begin{aligned} h^{\alpha\beta} &= \left[q + (1-q)\,\delta^{\alpha\beta}\right] h^{\beta} \\ h^{\beta} &= h_0 \left\{1 - \frac{s^{\beta}}{s^{0}}\right\}^{a} \\ h_0 = 180MPa \quad s_s &= 148MPa \quad a = 2.25 \end{aligned} \tag{2.55}$$

The parameter $q$ is set to 1 for coplanar slip systems and 1.4 for non-coplanar slip systems, as given by Anand [1], in order to be able to compare the results. However most of the simulations done in this study have been performed without hardening, by prescribing $h^{\beta} = 0$.

In order to determine the slip activity for the timestep, equation 2.53 and equation 2.54 are combined into equation 2.47. This combination gives a set of equations which are linear in $\Delta\gamma$, one equation for each potentially active slip system.

$$\sum_{\beta \in \mathscr{A}} A^{\alpha\beta} x^{\beta} = b^{\alpha} \tag{2.56}$$

$$A^{\alpha\beta} = h^{\alpha\beta}(t) + sgn\left(\tau^{\alpha}(\tau)^{tr}\right) sgn\left(\tau^{\beta}(\tau)^{tr}\right) \mathbf{S_0^{\alpha}} : \mathscr{C}\left[sym\left(\mathbf{C^e}(\tau)\,\mathbf{S_0^{\beta}}\right)\right] \tag{2.57}$$

$$b^{\alpha} = |\tau^{\alpha}(\tau)^{tr}| - s^{\alpha}(t) > 0 \tag{2.58}$$

$$x^{\beta} \equiv \Delta\gamma^{\beta} > 0 \tag{2.59}$$

It is shown by Anand [1] that solving the given set of equations using the Singular Value Decomposition(SVD) will give the solution of $\Delta\gamma^{\beta}$s with the smallest $L^2$ norm.

This corresponds closely to Taylors minimum virtual work criterion, as explained in the review by Manik and Holmedal [26].

When the system of equations is solved for the set $\mathscr{P}\mathscr{A}$, the solution should be checked to ensure that it is a valid solution. There are three main criteria that must be satisfied in order to march forward in time:

1. $\Delta\gamma^{\beta} < 0$

   This would be an non-physical solution. Systems for which this is the case are removed from the set of equations 2.56 and the calculation is redone on the new set. As proposed by Manik and Holmedal [26], in the case of multiple negative $\Delta\gamma^{\beta}$ the most negative is removed and the calculations are redone, until all $\Delta\gamma^{\beta}$ are positive.

2. Consistency on the active slip systems
   $|\tau^{\alpha}(\tau)| = s^{\alpha}(\tau)$ for $\alpha \in \mathscr{A}$

3. Non active systems have not been activated by slip activity.
   $|\tau^{\alpha}(\tau)| < s^{\alpha}(\tau)$ for $\alpha \notin \mathscr{A}$

The two last points can only be verified after both the slip resistance and resolved shear stress are updated using the plastic deformation gradient acquired from the calculated $\Delta\gamma^{\beta}$. If the two first criteria are violated, the respective system is removed from the set $\mathscr{P}\mathscr{A}$ and the calculation is redone. If the third criterion is violated, the respective system is added to $\mathscr{P}\mathscr{A}$ and, once again, the calculation is redone. When all checks are satisfied, the solution is accepted and the algorithm advances to the next time-step.

# 3 Implementation and validation of crystal plasticity model

The algorithm implemented is a semi-implicit algorithm, using the singular value decomposition(SVD) to find the appropriate set of slip systems. Holmedal and Manik [26] have shown that using SVD to find a solution for the slip increments correspond to Taylor's minimum of virtual work. This is due to the fact that the singular value decomposition returns the solution with the smallest $L_1$ norm, which in turn correspond to the smallest $L_2$ norm. The algorithm is presented in a step-wise manner in subsection 3.1 below. The material parameters used in the model is given in table 3.1 below.

**Table 3.1:** List of material parameters used for the crystal plasticity model

| Elasticity | | |
|---|---|---|
| $\mathscr{C}_{11} = 170\,[GPa]$ | $\mathscr{C}_{12} = 124\,[GPa]$ | $\mathscr{C}_{44} = 75\,[GPa]$ |
| Yield strength | | |
| $\tau_{crss} = 16\,[MPa]$ | | |
| Hardening | | |
| $h_o = 180\,[MPa]$ | $s_s = 148\,[MPa]$ | $a = 2.25$ |

## 3.1 Integration scheme

Initialization:

- Rotate the aggregate velocity gradient to the initial lattice frame:
  $\mathbf{L_c} = \mathbf{Q_0 L_a Q_0^T}$
  Where $\mathbf{Q_0}$ is the rotation matrix from the aggregate to the initial lattice frame.
- If the algorithm is initialized for the first time, $\mathbf{F}(\mathbf{0}), \mathbf{F^p}(\mathbf{0})$ and $s^\alpha(0)$ must be initialized
  $\mathbf{F}(0) = \mathbf{I}$
  $\mathbf{F^p}(0) = \mathbf{I}$

$s^{\alpha}(0) = 16$ [MPa]

Algorithm:

1. Calculate the new total deformation gradient $\mathbf{F}(\tau)$

   $\mathbf{F}(\tau) = [\mathbf{I} + \mathbf{L_c}\Delta t]\,\mathbf{F}(\mathbf{t})$

2. Calculate the trial elastic deformation gradient $\mathbf{F^e}(\tau)^{\mathbf{tr}}$

   $\mathbf{F^e}(\tau)^{\mathbf{tr}} = \mathbf{F}(\tau)\,\mathbf{F^{-p}}(\mathbf{t})$

3. Calculate the trial elastic strain, $\mathbf{E^e}(\tau)^{\mathbf{tr}}$

   $\mathbf{C^e}(\tau)^{\mathbf{tr}} = \left(\mathbf{F^e}(\tau)^{\mathbf{tr}}\right)^{\mathbf{T}}\mathbf{F^e}(\tau)^{\mathbf{tr}}$

   $\mathbf{E^e}(\tau)^{\mathbf{tr}} = \frac{1}{2}\left(\mathbf{C^e}(\tau)^{\mathbf{tr}} - \mathbf{I}\right)$

4. Detemine the trial second Piola-Kirchoff stress, $\mathbf{T}^{*}(\tau)^{\mathbf{tr}}$

   $\mathbf{T}^{*}(\tau)^{\mathbf{tr}} = \mathscr{C}\left[\mathbf{E^e}(\tau)^{\mathbf{tr}}\right]$

5. Compute the trial resolved shear stress, $\tau^{\alpha}(\tau)^{tr}$

   $\tau^{\alpha}(\tau)^{tr} = \mathbf{T}^{*}(\tau)^{\mathbf{tr}} : \mathbf{S_0^{\alpha}}$

   for all $\alpha$

6. Determine the set of potentially active slip systems, $\mathscr{PA}$.

   $|\tau^{\alpha}(\tau)^{tr}| > s^{\alpha}(t) \Rightarrow \in \mathscr{PA}$

7. Calculate slip increments by solving the consistency equation.

   For all $\alpha \in \mathscr{PA}$ :

$$A^{\alpha\beta} = h^{\alpha\beta}(t) + sgn\left(\tau^{\alpha}(\tau)^{tr}\right) sgn\left(\tau^{\beta}(\tau)^{tr}\right)\mathbf{S_0^{\alpha}} : \mathscr{C}\left[sym\left(\mathbf{C^e}(\tau)^{tr}\,\mathbf{S_0^{\beta}}\right)\right]$$

$$b^{\alpha} = |\tau^{\alpha}(\tau)^{tr}| - s^{\alpha}(t)$$

$$\mathbf{A}\Delta\boldsymbol{\gamma} = \mathbf{b}$$

   Which is solved using the SVD method. If for any $\alpha$ the calculated $\Delta\gamma^{\alpha} \leq 0$, the slip system is removed from the set $\mathscr{PA}$ and the step is repeated. This is done until all $\Delta\gamma$'s are positive. If multiple $\Delta\gamma$'s are negative, the most nega-

tive is removed.

8. Calculate the new plastic deformation gradient using the acquired $\Delta\gamma$

   $$\mathbf{F^p}(\tau) = \left\{\mathbf{I} - \sum_{\alpha\in\mathscr{A}} sgn\left(\tau^\alpha(\tau)\right)\Delta\gamma^\alpha \mathbf{S_0^\alpha}\right\}\mathbf{F^p}(t)$$

   Check that the determinant of $\mathbf{F^p}(\tau) = 1$. If not $\mathbf{F^p}(\tau)$ should be normalized.

   $$\mathbf{F^p}(\tau) = \left[det\left(\mathbf{F^p}(\tau)\right)\right]^{-\frac{1}{3}}\mathbf{F^p}(\tau)$$

9. Calculate updated elastic deformation gradient and Second Piola-Kirchoff stress.

   $$\mathbf{F^e}(\tau) = \mathbf{F}(\tau)\,\mathbf{F^{-p}}(\tau)$$

   $$\mathbf{T}^*(\tau) = \mathbf{T}^*(\tau)^{\mathbf{tr}} - \sum_{\alpha\in\mathscr{A}} sgn\left(\tau^\alpha(\tau)^{tr}\right)\Delta\gamma^\alpha\ \mathscr{C}\left[sym\left(\mathbf{C^e}(\tau)^{tr}\,\mathbf{S_0^\beta}\right)\right]$$

10. Update Cauchy stress and critical resolved shear stress, $\mathbf{T}(\tau)$ and $s^\alpha(\tau)$.

    $$\mathbf{T}(\tau) = \mathbf{F^e}(\tau)\left\{det\left(\mathbf{F^e}(\tau)\right)^{-1}\mathbf{T}^*(\tau)\right\}\mathbf{F^e}(\tau)^T$$

    $$s^\alpha(\tau) = s^\alpha(t) + \sum_{\beta\in\mathscr{A}} h^{\alpha\beta}(t)\,\Delta\gamma^\beta$$

    Naturally, $s^\alpha(\tau)$ is updated for all slip systems of the crystal. Due to latent hardening even non slipping systems will harden.

11. Check that consistency is achieved. The first point of validating the solution is taken care of in step 7, but the remaining two points still need verification:

    - Consistency on the active slip systems
      $|\tau^\alpha(\tau)| = s^\alpha(\tau)$ for $\alpha \in \mathscr{A}$
    - Non-active systems have not been activated by slip activity.
      $|\tau^\alpha(\tau)| < s^\alpha(\tau)$ for $\alpha \notin \mathscr{A}$

12. Update the lattice orientation and rotate the Cauchy stress to the aggregate frame.

    The lattice rotation is incorporated in $\mathbf{F^e}(\tau)$, which can be decomposed by polar decomposition.

$$\mathbf{F^e} = \mathbf{R^e}\,(\tau)\,\mathbf{U^e}\,(\tau)$$

$$\mathbf{Q}\,(\tau) = \mathbf{R^e}\,(\tau)^T\,\mathbf{Q_0}$$

The Cauchy stress is given in the initial lattice frame and can be transformed into the aggregate frame by:

$$\mathbf{T_a} = \mathbf{Q_0^T T}\,(\tau)\,\mathbf{Q_0}$$

Here the stress state of the aggregate is determined as the average over all grains.

## 3.2 Validation of the crystal plasticity model

This section is more or less copied directly from the authors project thesis, since the report is not available to the public, the section is added for the sake of completenes. In order to validate the crystal plasticity model several meassures have been made. First, single crystal tensile tests have been calculated, which at least in part replicate the tests performed by Anand and Kothari [1]. If the model implemented replicates the results originally acquired, the model is considered to be validated. Texture development has been calcuated to verify that the model produces the same texture as expected for an fcc material. The last verification done, is calculating the power of the produced yield surface for an isotropic fcc metal, which according to Barlat [4] should be $n = 8.95$.

### 3.2.1 Single crystal tensile tests

Single crystal tensile tests have been simulated for three different Euler angles, the same angles which were used by Anand and Kothari [1]. The angles are listed in table 3.2. The boundary conditions used by Anand and Kothari to simulate the tensile tests corresponds to allow horizontal displacement of the connection between the tensile specimen and the loading machine, while keeping the ends of the specimen perpendicular to the tensile axis. However this is not a straight forward simulation to do, as the velocity gradient is not apriori determined, and an iterative alogrithm is needed in order to perform the

simulation. However, for stretching in [001] and [111] directions, the symmetry cancels out all horizontal displacements. As a consequence, the results will align with the constrained tensile test performed by using the velocity gradient given in equation 3.1. The simulation done for a tensile test in the [236] direction will however not be the same. As the simulation does not allow any sideways motion of the attachment points between the specimen and the loading machine, more slip system must be activated earlier on.

$$L_a = \begin{bmatrix} -0.0005 & 0 & 0 \\ 0 & -0.0005 & 0 \\ 0 & 0 & 0.001 \end{bmatrix} \tag{3.1}$$

**Table 3.2:** Single crystal orientations specified by Bunge Euler angles, presented in radians. Conversion of Euler angles are taken from Kalidindi [18]

| Orientation | $\phi_1$ | $\Phi$ | $\phi_2$ |
|---|---|---|---|
| [001] | 0 | 0 | 0 |
| [111] | 0 | 0.9553164 | $\pi/4$ |
| $[\bar{2}36]$ | 0 | −0.5410521 | 2.5534167 |

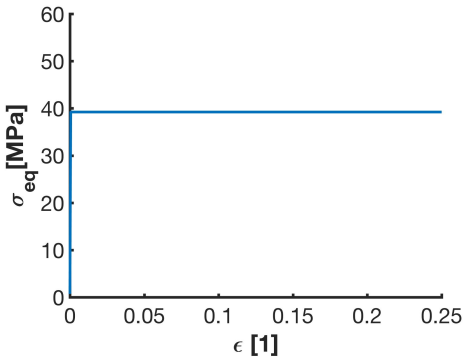


**(a)** Stress-strain plot for volume conserving tension in the [001] direction, to a tensile strain of $\epsilon = 0.25$. Note that the stress is given as von Mises equivalent stress.

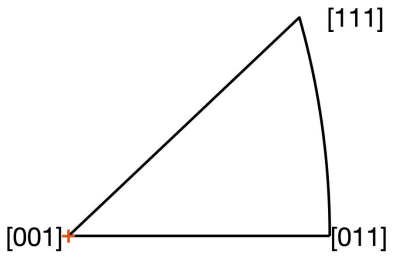


**(b)** Inverse pole figure to show that the crystal is not rotating, when it is stretched in the [001] direction. Strain to $\epsilon = 0.25$

**Figure 3.1:** Stress strain curve and inverse pole figure, for [001] single crystal strained to $\epsilon = 0.25$ in volume conserving tension.

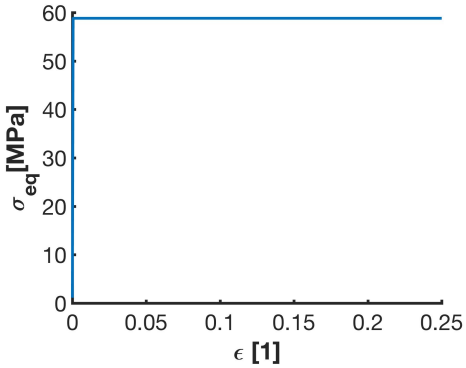


**(a)** Stress-strain plot for volume conserving tension in the [111] direction, to a tensile strain of $\epsilon = 0.25$. Note that the stress is given as von Mises equivalent stress.

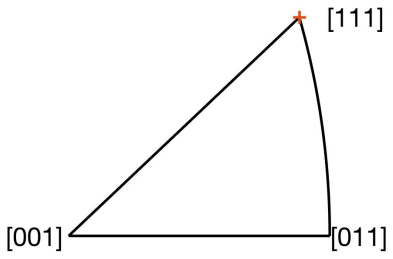


**(b)** Inverse pole figure to show that the crystal is not rotating, when it is stretched in the [111] direction. Strain to $\epsilon = 0.25$

**Figure 3.2:** Stress strain curve and inverse pole figure, for [111] single crystal strained to $\epsilon = 0.25$ in volume conserving tension.

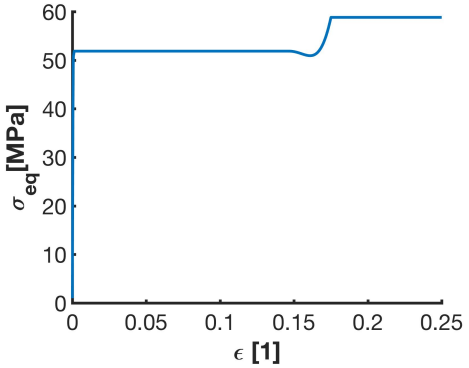


**(a)** Stress strain plot for volume conserving tension in [236] direction, to a tensile strain of $\epsilon = 0.25$. Note that the stress is given as von Mises equivalent stress.

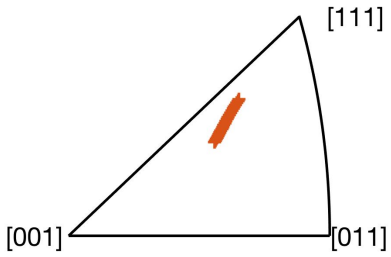


**(b)** Inverse pole figure showing the crystal rotation up to a strain of $\epsilon = 0.25$

**Figure 3.3:** Stress strain curve and inverse pole figure, for a single crystal strained in the [236] direction to $\epsilon = 0.25$ in a volume conserving tensile test.

As can be seen from the plots in figures 3.1, 3.2 and 3.3, the [011] and [111] are stable directions in tensile loading. However the [236] direction is not stable and rotates towards the [111] corner of the triangle in the standard (100) prosjection. As explained, it is not expected that the [236] direction would behave in the same way as in the results presented by Anand and Kothari. However the grain rotation seems to be in agreement with the rotation field presented in the paper by Mánik and Holmedal [26], for which the same velocity gradient is used.

The von Mises equivalent strain is not necessarily a good stress measure for single crystals, but since it seems to be the one used by Anand and Kothari it is used for these tensile tests, in order to be able to compare. The jump in equivalent stress for the [236] direction, shown in figure 3.3a, is due to a transition from one set of active slip systems to another. Any non symmetrical set of active slip systems must eventually evolve into a symmetric set, with respect to the tensile axis. Apparently in von Mises equivalent stress, the jump appears non smooth. The same experiment have been performed using another, independent,

rigid plastic polycrystal plasticity model, as described by Manik and Holmedal [26], with the same result. This support the validity of the implemented model.

Based on the results above there is no reason to believe that the model is incorrect. The results for the two symmetrical orientations are the same as those of Anand and Kothari. The tests for the [236] direction have been compared to another rigid-plastic crystal plasticity model which gives the same results.

### 3.2.2 Texture development

Another route to validation of the model is to do texture development simulations. It is well known what are the typical texture components of fcc metals in for instance rolling. These typical textures may be compared with the textures acquired by simulations. For the rolling simulations a set of 936 uniformly distributed orientations is used.

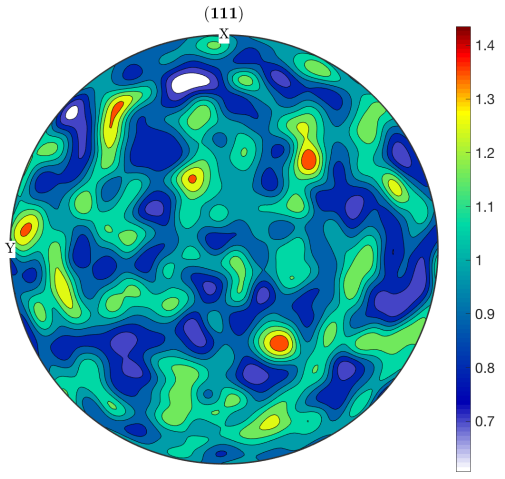


**(a)** (111) pole figure of the uniformly distributed orientations. The vertical axis is the rolling direction and the horizontal axis is the transversal direction.

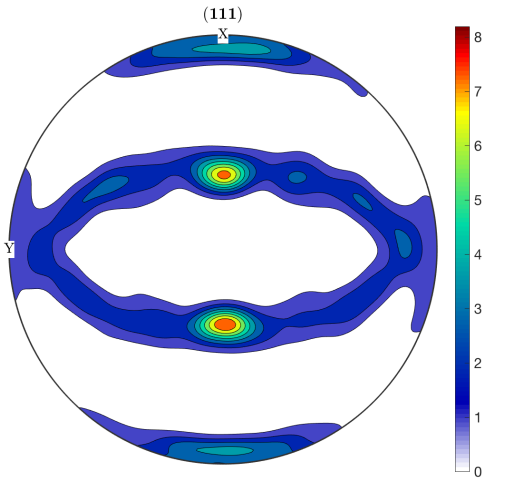


**(b)** (111) pole figure of crystal aggregate rolled to $\epsilon = 1$. The vertical axis is the rolling direction and the horizontal axis is the transversal direction.

**Figure 3.4:** [111] pole figure of crystal aggregate before and after rolling to a strain of $\epsilon = 1$. Both polefigures are plotted using the Mtex toolkit in Matlab.

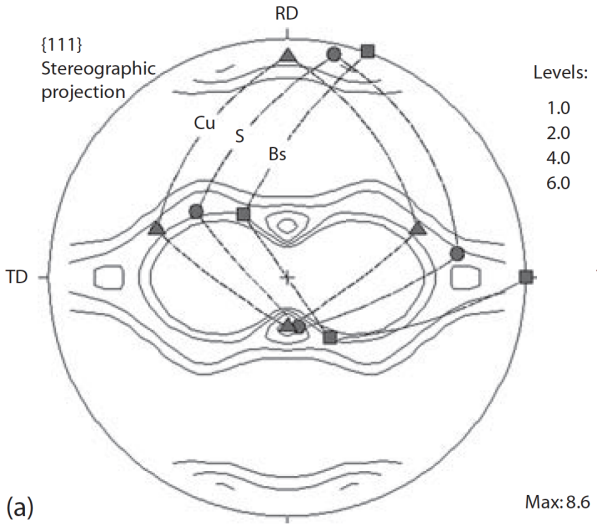


**Figure 3.5:** {111} Polefigure showing the common texture for pure copper. The Cu, S and Brass texture components are also plotted. The figure is taken from figure 5.15 on page 148, of the book "Introduction to Texture Analysis" by Olaf Engler and Valerie Randle [12].

The texture acquired is recognized as the texture typical for pure rolled copper, as can be seen by comparing the calculated polefigure, with the one given in figure 3.5, taken from the book "Introduction to Texture Analysis" by Olaf Engler and Valerie Randle [12]. This result further supports that the model is valid.

The set of grains used for the texture evolution simulations is the same set of uniformly distributed grains as are used for the polycrystal experiments, hence the polefigure of the uniformly distributed grains is taken as a validation that the orientations are close to uniformly distributed. Some peaks with increased intensity are seen, but one should note that the scale is different between the two polefigures. Hence these variations are small.

### 3.2.3 Yield surfaces

The model has been used to calculate yield surfaces for a uniformly distributed set of grain orientations, which should give close to isotropic properties. As explained in the preceding chapters, the yield surface is dependent on the plastic work performed. The

saturated yield surface has been fitted to a Hosford yield surface [17] and the power is determined to be, $n = 8.9995$. Which is consistent with the results of Barlat [4], who have determined the yield surface power to be $n = 8.95$ for an fcc material using crystal plasticity simulations from an FC-Taylor model [4]. The deviation shown is small, and could be caused by a lot of different factors, for instance elasticity. It is therefore reasonable to conclude that the result supports the validity of the model.

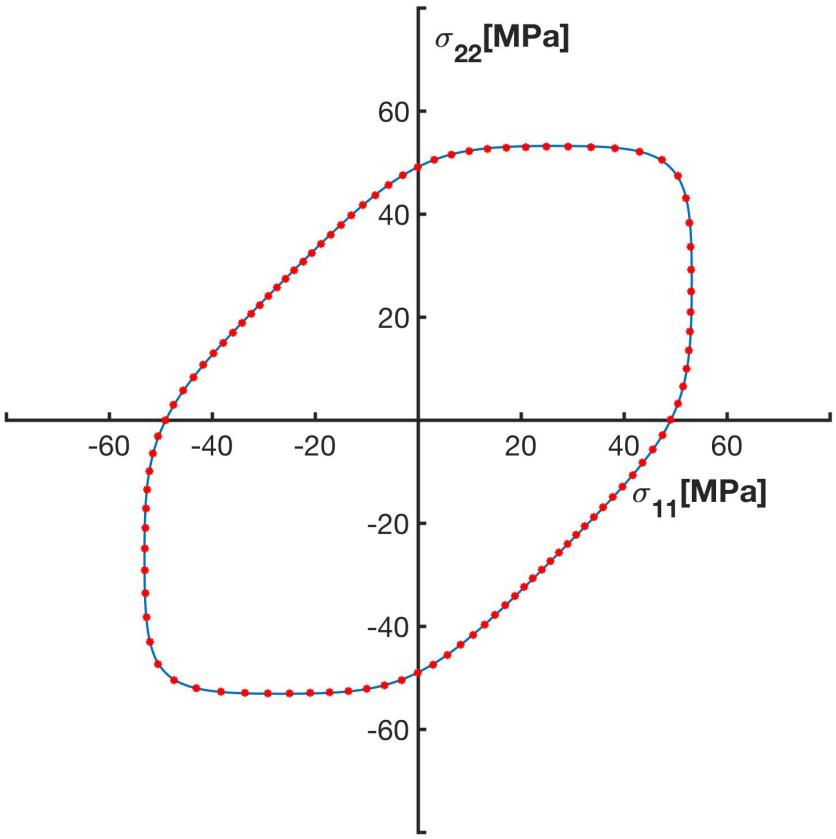


**Figure 3.6:** Calculated yield surfaces of $\bar{\epsilon}_{vM} = 0.02$ have been fitted to a Hosford yield surface of power $n = 8.9995$, both are plotted in the figure above. The yield strength is determined to be 49.103MPa. The computed yield surface is plotted as a blue line and the Hosford surface by red dots.

The tensile yield strength of the material is determined to be 49.103 MPa, at an offset strain of $\bar{\epsilon}_{vM} = 0.02$. Since the critical resolved shear stress, $\tau_{CRSS} = 16$ MPa is used,

the Taylor factor, $M = \frac{\sigma_{eq}}{\tau_{CRSS}}$, is calculated to be $M = 3.07$. Which is in line with the established value of the Taylor factor for random textures of $M = 3.07$, which recently have been verified in the works of Zhang et al. [37]. The fitted and the calculated surface are plotted in figure 3.6 for comparison.

# 4 Implementation of constitutive equation

## 4.1 Integration scheme

The phenemenological plasticity model implemented is adapted from Yoshida [36] [34]. Such a constitutive relation is based on three main consistuents, a flow rule, a hardening law and a yield surface. In addition an unloading-loading criterion should be formulated. These constituents are originally presented in section 2.7, but is briefely reviewed in this section.

The flow rule used in the model is given by equation 4.1. It is decomposed into a tangential and a normal component. The hardening relation proposed by Yoshida [34] has been adapted and is given by equation 4.2.

$$\mathbf{D}^p = \mathbf{D}^p_n + \mathbf{D}^p_t = \dot{\lambda}\mathbf{N} + \alpha \mathbf{D'}_t \tag{4.1}$$

$$g\left(\bar{\epsilon}^p_n\right) = \sigma_0\Big(1 + \frac{\bar{\epsilon}^p}{\epsilon_0}\Big)^n \tag{4.2}$$

The yield surface used in the model is a Hoshford/Hershey isotropic yield surface [17]. The power have been determined to $n = 8.9995$ from the crsytal plasticity simulations. The yield surface has two applications in the constitutive model, firstly it is used to determine the equivalent stress at the given loading point, and secondly the yield surface is used to calculate the normal of the yield surface. For an isotropic Hoshford surface, Barlat [5] has derived an analytic formulation in all six stress components, listed in equation 4.3 through equation 4.7. This formulation has been used to calculate the equivalent stress from the stress tensor. The derivative of the expression is calculated to find an analytic expression for the yield surface normal. This derivation is quite lengthy and is given in appendix A.

$$A = \sigma_{22} - \sigma_{33} \qquad B = \sigma_{33} - \sigma_{11} \qquad C = \sigma_{11} - \sigma_{22} \tag{4.3}$$
$$F = \sigma_{23} \qquad G = \sigma_{13} \qquad H = \sigma_{12}$$

$$I_2 = \frac{F^2 + G^2 + H^2}{3} + \frac{(A-C)^2 + (C-B)^2 + (B-A)^2}{54} \tag{4.4}$$

$$I_3 = \frac{(C-B)(A-C)(B-A)}{54} + FGH - \frac{(C-B)F^2 + (A-C)G^2 + (C-B)H^2}{6} \tag{4.5}$$

$$\Theta = \arccos\left(\frac{I_3}{I_2^{3/2}}\right) \tag{4.6}$$

$$2\bar{\sigma}^m = (3I_2)^{m/2}\left\{\left[2\cos\left(\frac{2\Theta+\pi}{6}\right)\right]^m + \left[2\cos\left(\frac{2\Theta-3\pi}{6}\right)\right]^m - \left[2\cos\left(\frac{2\Theta+5\pi}{6}\right)\right]^m\right\} \tag{4.7}$$

The algorithm proposed by Yoshida, uses an elastoplastic moduli to calculate the objective stress rate at each timestep and integrate forward in time, as indicated in section 2.7. In addition to beeing an explicit integration scheme, this formulation is also rate controlled. At the current position the stress rate direction needed to maintain consistency is calculated, and the stress is updated in this direction. Consequently there is no control of whether the solution have drifted from consistency or not. At least in the implementation of the explicit formulation done in this study the solution drifted from consistency quite rapidly, especially after a strain path change, which is the phenomenon of interest. To ensure that consistency is maintained, an implicit algorithm using an elastic predictor and a plastic corrector has been implemented. The implicit scheme does not rely on rates, and ensures that the consistency equation is satisfied at the end of each time-step. The elastic predictor is computed by assuming that the full deformation step is elastic, hence $\mathbf{D} = \mathbf{D}^e$. The trial elastic stress is then defined according to equation 4.8

$$\begin{aligned} \mathring{\boldsymbol{\sigma}}_{n+1}^{trial} &= \mathscr{C}^e\left[\mathbf{D}_n\right] \\ \boldsymbol{\sigma}_{n+1}^{trial} &= \boldsymbol{\sigma} + \mathscr{C}^e\left[\mathbf{D}_n\right]\Delta t \end{aligned} \tag{4.8}$$

$$\begin{aligned} &\bar{\sigma}^{trial}\left(\boldsymbol{\sigma}_{n+1}^{trial}\right) < g\left(\bar{\epsilon}_n^p\right) \Rightarrow \text{Elastic solution accepted} \\ &\bar{\sigma}^{trial}\left(\boldsymbol{\sigma}_{n+1}^{trial}\right) \geq g\left(\bar{\epsilon}_n^p\right) \Rightarrow \text{Calculate plastic corrector} \end{aligned} \tag{4.9}$$

If the deformation step is fully elastic, there is no change in the plastic strain and the critical yield strength, and consequently the consistency condition may be checked directly. If the computed trial equivalent stress is less than the critical yield stress, the elastic solution is accepted. However if the trial equivalent stress is larger, a plastic corrector step must be performed. Such a step is calculated through solving the set of equations 4.10.

$$\begin{aligned} 0 &= \boldsymbol{\sigma}_{n+1} - \boldsymbol{\sigma}_n^{trial} - \mathring{\boldsymbol{\sigma}}_{n+1}^{plastic}\Delta t \\ 0 &= \bar{\sigma}\left(\boldsymbol{\sigma}_{n+1}\right) - g\left(\bar{\epsilon}_{n+1}^p\right) \end{aligned} \tag{4.10}$$

To fill inn the equations the set of relations given in 4.11 is used. Since the elastic predictor step has already been calculated, the computed value is used throughout the calculation. For a given $\mathring{\boldsymbol{\sigma}}_{n+1}$ and $\dot{\lambda}_{n+1}$ the differences in equations 4.10 is calculated. If the deviation from zero in any of the seven equations is above the prescribed threshold, a numerical algorithm is used to solve the set of equations.

$$\begin{aligned} \mathring{\boldsymbol{\sigma}}_{n+1}^{plastic} &= -\mathscr{C}^e\left[\mathbf{D}_{n+1}^p\right] \\ \mathbf{D}_{n+1}^p &= \dot{\lambda}_{n+1}\mathbf{N}_{n+1} + \alpha\mathbf{D}'_{t(n+1)} \\ \dot{\bar{\epsilon}}_{n+1}^p &= \dot{\lambda}_{n+1}\sqrt{\frac{2}{3}}||\mathbf{N}_{n+1}|| \\ \bar{\epsilon}_{n+1}^p &= \bar{\epsilon}_n^p + \dot{\bar{\epsilon}}_{n+1}^p\Delta t \\ \mathbf{N}_{n+1} &= \frac{\partial\bar{\sigma}}{\partial\boldsymbol{\sigma}}\left(\boldsymbol{\sigma}_{n+1}\right) \\ g\left(\bar{\epsilon}_{n+1}^p\right) &= \sigma_0(1 + \frac{\bar{\epsilon}_{n+1}^p}{\epsilon_0})^n \end{aligned} \tag{4.11}$$

The set of equations 4.10 is regarded as seven equation in seven variables, six stress components and the plastic consistency parameter. The system of equations is solved using the Newton-Raphson method, according to equation 4.12, where $\mathbf{J}_F$ is the jacobian, $\mathbf{x}$ is the current value of the variables $\mathring{\boldsymbol{\sigma}}_{n+1}$ and $\dot{\lambda}_{n+1}$ and $\mathbf{F}(\mathbf{x}_n)$ is the calculated differences for the current $\mathbf{x}$. The Jaobian is calculated numerically by a forward difference.

$$\mathbf{J}_F \Delta \mathbf{x} = -\mathbf{F}(\mathbf{x}_n) \tag{4.12}$$

If the differences given by equations 4.10 is below a given threshold, the solution is accepted and the variables updated.

## 4.2 Calibration of the elastic modulus

The isotropic elastic modulus of the yield surface must be determined for the actual crystal for which the simulations are to be done. This is achieved through performing an elastic step using the crystal plasticity model. Since the number of grains is large and the orientations close to uniformly distributed it is assumed that the behaviour is isotropic, even though the modulus of elasticity for each of the crystals is orthotropic. Hence an elastic step is performed, and the elastic parameters are determined using Voigt notation, according to equation 4.13.

$$\boldsymbol{\sigma} = \begin{bmatrix} 2G+\lambda & \lambda & \lambda & 0 & 0 & 0 \\ \lambda & 2G+\lambda & \lambda & 0 & 0 & 0 \\ \lambda & \lambda & 2G+\lambda & 0 & 0 & 0 \\ 0 & 0 & 0 & G & 0 & 0 \\ 0 & 0 & 0 & 0 & G & 0 \\ 0 & 0 & 0 & 0 & 0 & G \end{bmatrix} \begin{bmatrix} E_{11} \\ E_{22} \\ E_{32} \\ 2E_{23} \\ 2E_{13} \\ 2E_{12} \end{bmatrix} \tag{4.13}$$

Hence for a deformation in the elastic range the material should follow the given stress strain relation, and since both the stress, $\boldsymbol{\sigma}$, and the strain, $\mathbf{E}$, are known, the elastic parameters, $G$ and $\lambda$ may be determined.

## 4.3 Calibration of the hardening curve

The hardening law given in equation 2.20 in section 2.7, has been fitted to data acquired from an uniaxial tension experiment simulated using the crystal plasticity model. The produced stress and strain have been imported into Microsoft Excel, and solver has been used to fit the parameters $\epsilon_0$ and $n$. The yield stress is calculated by performing a simulation to a strain equal to the offset strain for the yield surface in question. For instance, following Yoshida [34], the strain path changes have been performed at a strain of $\bar{\epsilon}^p = 0.02$, and consequently this has been used as the offset strain.

# 5 Framework for virtual experiments

In order to use the model to perform virtual experiments, an additional framework is needed to ensure that the boundary conditions of the experiment are full-filled at all times. For instance, for a uniaxial tensile test, all stresses should be zero, except the stress in the tensile direction. Hence for each timestep, this condition must be verified, if the deviation from this boundary condition is above a prescribed threshold, the input to the model, usually the components of the velocity gradient, must be altered such that the boundary condition is satisfied at the end of the timestep.

Two different sets of boundary conditions have been implemented. Both stress and strain control have been implemented in the $\sigma_{11}$ - $\sigma_{22}$ plane. In strain control the deformation rate in the 11 and 22 direction is prescribed, the remaining components of the velocity gradient are adjusted such that all stress components, except $\sigma_{11}$ and $\sigma_{22}$, are zero. The set of equations which must be solved to fulfill this boundary condition, is given in equation 5.1. The question-marks represent unknown variables, which have to be determined.

$$\mathbf{L} = \begin{bmatrix} L_{11} & ? & ? \\ ? & L_{22} & ? \\ ? & ? & ? \end{bmatrix} \Rightarrow Model \Rightarrow \boldsymbol{\sigma} = \begin{bmatrix} ? & 0 & 0 \\ 0 & ? & 0 \\ 0 & 0 & 0 \end{bmatrix} \tag{5.1}$$

In order for the system of equations to be solved, it is assumed that the velocity gradient is symmetric, which makes $\mathbf{L} = \mathbf{D}$. Without this assumption, due to the ineherent symmetry of the cauchy stress tensor, there would be four equations and seven unknowns, hence the system would be under-determined. To solve the equations each of the four independent stress components, $\sigma_{33}$, $\sigma_{23}$, $\sigma_{13}$ and $\sigma_{12}$ is regarded as functions of the the four free components of the deformation rate, according to equaion 5.2.

$$\begin{aligned} \sigma_{33}\left(D_{33}, D_{23}, D_{13}, D_{12}\right) &= 0 \\ \sigma_{23}\left(D_{33}, D_{23}, D_{13}, D_{12}\right) &= 0 \\ \sigma_{13}\left(D_{33}, D_{23}, D_{13}, D_{12}\right) &= 0 \\ \sigma_{12}\left(D_{33}, D_{23}, D_{13}, D_{12}\right) &= 0 \end{aligned} \tag{5.2}$$

The resulting set of equations is solved using Newton-Raphson iterations. The Jacobian is determined numerically using a forward difference. A central difference scheme has also been implemented, but the extra computations needed were deemed not to be worth the improved precision.

When experiments are performed in stress control, the boundary value is slightly different. In this case, all the stress components have a target relative to $\sigma_{11}$ or $\sigma_{22}$, the stress direction is given by a six-component vector in the stress space. At least one stress component must be kept free, and the other is proportional to the free stress variable. For instance in biaxial loading, where $\sigma_{11} = \sigma_{22}$ and all other stresses zero, the proportionality constant for $\sigma_{22}$ is 1 with respect to $\sigma_{11}$. It is clear that if $\sigma_{11}$ is kept free while performing a tensile test in the $\sigma_{22}$ direction, the proportionality constant would diverge to infinity. It has been found that there are convergence issues when solving the boundary condition when the proportionality constant is much larger than one. To circumvent this issue the $\sigma_{11}$ - $\sigma_{22}$ stress space has been divided into two regions, indicated in figure 5.1. The criterion is based on the absolute values of $\sigma_{11}$ and $\sigma_{22}$. If $|\sigma_{11}|$ is greater or equal to $|\sigma_{22}|$ then $\sigma_{11}$ is the free variable, and oppositely $\sigma_{22}$ is kept free if $|\sigma_{11}|$ is less than $|\sigma_{22}|$.

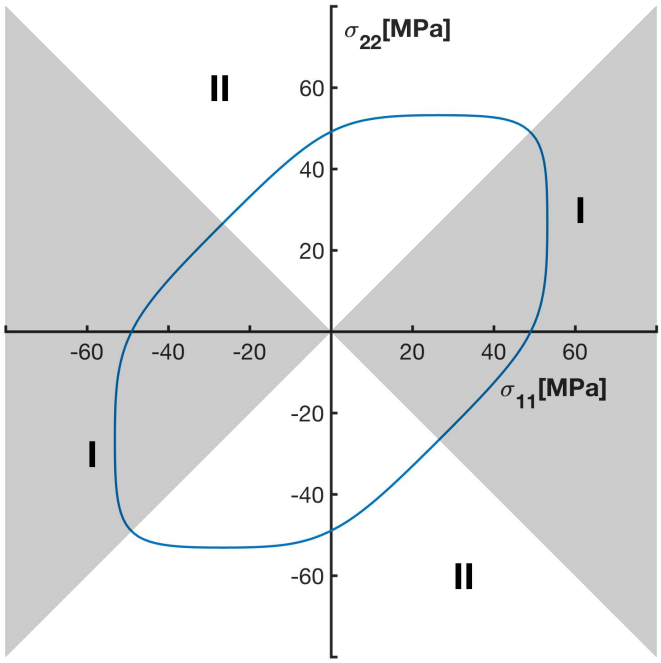


**Figure 5.1:** The regions where the stress is related to $\sigma_{11}$ is shaded in gray, and marked I. The white regions, marked II is the regions where $\sigma_{22}$ is the free stress variable. Separating a stress direction is actually only dependent on one criterion, which is why there is only two regions. The white regions are where $|\sigma_{11}| < |\sigma_{22}|$ and the grey where $|\sigma_{11}| \leq |\sigma_{22}|$.

As is apparent from equation 5.3, the system now consists of five equations and unknowns, written out in equation 5.4. The equations are written in the form where $\sigma_{11}$ is the free variable.

$$\mathbf{L} = \begin{bmatrix} L_{11} & ? & ? \\ ? & ? & ? \\ ? & ? & ? \end{bmatrix} \Rightarrow Model \Rightarrow \boldsymbol{\sigma} = \begin{bmatrix} ? & k_1\sigma_{11} & k_2\sigma_{11} \\ k_1\sigma_{11} & k_5\sigma_{11} & k_3\sigma_{11} \\ k_2\sigma_{11} & k_3\sigma_{11} & k_4\sigma_{11} \end{bmatrix} \tag{5.3}$$

$$\begin{aligned}
\sigma_{33}\left(D_{33}, D_{23}, D_{13}, D_{12}, D_{22}\right) - k_4\sigma_{11}\left(D_{33}, D_{23}, D_{13}, D_{12}, D_{22}\right) &= 0 \\
\sigma_{23}\left(D_{33}, D_{23}, D_{13}, D_{12}, D_{22}\right) - k_3\sigma_{11}\left(D_{33}, D_{23}, D_{13}, D_{12}, D_{22}\right) &= 0 \\
\sigma_{13}\left(D_{33}, D_{23}, D_{13}, D_{12}, D_{22}\right) - k_2\sigma_{11}\left(D_{33}, D_{23}, D_{13}, D_{12}, D_{22}\right) &= 0 \\
\sigma_{12}\left(D_{33}, D_{23}, D_{13}, D_{12}, D_{22}\right) - k_1\sigma_{11}\left(D_{33}, D_{23}, D_{13}, D_{12}, D_{22}\right) &= 0 \\
\sigma_{22}\left(D_{33}, D_{23}, D_{13}, D_{12}, D_{22}\right) - k_5\sigma_{11}\left(D_{33}, D_{23}, D_{13}, D_{12}, D_{22}\right) &= 0
\end{aligned} \tag{5.4}$$

The experiments then obey the boundary condition until a desired strain is reached. To increase the precision of the desired strain at which the experiment is ended, an algorithm adjusting the timestep has been developed. If the target strain is superseded, interpolation is used to approximate a more appropriate timestep and the deformation step is redone. This process is repeated until the calculated strain is within a given margin of the target strain. The update formula is given in equation 5.5. In the original version of the algorithm, the timestep was accepted if the strain was below the target strain, making the distance to the target smaller and smaller, however these very small time steps caused issues when trying to solve the boundary value problem, and the algorithm did not converge. To circumvent this issue, the timestep is never accepted before the desired strain is within the tolerances, to make sure that longer time steps are used, while still achieving the desired precision.

$$\Delta t = \frac{\epsilon_{target} - \epsilon_{calc}}{\epsilon_{calc} - \epsilon_{current}} \Delta t_{current} \tag{5.5}$$

The precision problems caused by small timesteps are related to the crystal plasticity algorithm, as there is no possibility to iterate on the solution to increase the numerical accuracy. Hence if a deformation field with zero deformation is passed to the algorithm the solution will be slightly different. Implementing an iterative procedure to the crystal plasticity algorithm would be a desired upgrade. It must however be emphasized that this inaccuracy is only a problem at timesteps below $\approx 10^{-12}$ or smaller, and hence it is in a range close to the machine precision of ordinary computers.

In order to illustrate the overall flow of the virtual experiment framework, the algorithm is presented in the flowchart in figure 5.2. The input-output parameters, $\mathbf{F}_0$, $\mathbf{F}_{p0}$ and $\mathbf{S}_0$ are only relevant for the crystal plasticity model. For the constitutive model only $\epsilon_p$ and $\boldsymbol{\sigma}$ are input and output.

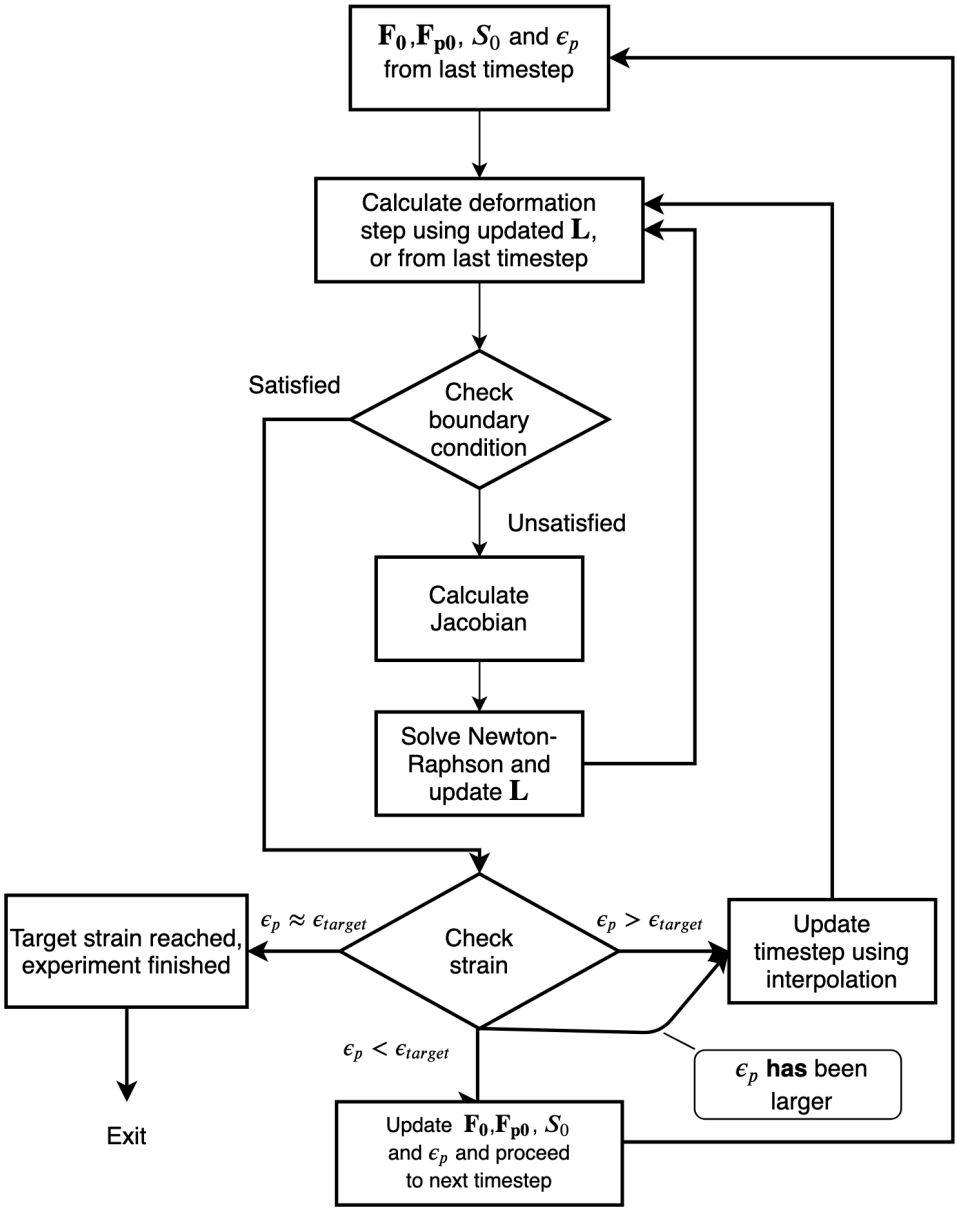


**Figure 5.2:** Flowchart of the boundary condition algorithm, the code has options to choose between the two types of boundary condition and the desired target strain. There is also options to write out various data during the experiment.

# 6 Fitting of model parameters

In order to fit the model parameters which best fit the data acquired from the crystal plasticity simulations, an optimization algorithm has been implemented. First of all, a suitable measure of the distance between the two models must be chosen, in order to have a quantity to minimize. In this case, the angle between the deviatoric stress points, at equal strains, has been used as the quantitative measure. Minimizing the distance between the stress points will make the two models slide along the yield surface at a similar speed.

Further, the set of stress-strain points to use in the optimization must be chosen. In this case it is essential that the set of points is selected such that all parts of the model are taken into account. It is important that some points right after the strain path change, where $\theta$ is large, must be taken into account. If $\theta$ is always smaller than $\theta_{crit}$, a change in $\theta_{crit}$ will not make any difference on the deviation measure. Further, some points at larger strains beyond the strain path change must be taken into account in order to optimize the coefficients $c_1$ and $c_2$. The set of points used are five points with $\Delta\bar{\epsilon}^p = 0.00005$ and ten points with $\Delta\bar{\epsilon}^p = 0.0005$ according to table 6.1.

**Table 6.1:** List of strain for the points used for fitting model parameters. The strain path change is performed at $\bar{\epsilon}^p = 0.02$ as in the simulations provided by Yoshida [34]. As can be seen from the first column, five small steps are performed, then ten large, with one intermediate step.

| # | $\bar{\epsilon}^p$ | # | $\bar{\epsilon}^p$ | # | $\bar{\epsilon}^p$ |
|---|---|---|---|---|---|
| 1 | 0.02+0.00005 | 6 | 0.02+0.0005 | 11 | 0.02+0.0030 |
| 2 | 0.02+0.00010 | 7 | 0.02+0.0010 | 12 | 0.02+0.0035 |
| 3 | 0.02+0.00015 | 8 | 0.02+0.0015 | 13 | 0.02+0.0040 |
| 4 | 0.02+0.00020 | 9 | 0.02+0.0020 | 14 | 0.02+0.0045 |
| 5 | 0.02+0.00025 | 10 | 0.02+0.0025 | 15 | 0.025 |

The total deviation is then calculated according to equation 6.1, where $\mathbf{s}_i^{con}$ is the devi-

atoric stress for point #1 of the constitutive model, $\mathbf{s}_i^{cp}$ is the same quantity from the crystal plasticity model and $n$ is the number of stress points.

$$\text{error}\left(c_1, c_2, c_3, \theta_{crit}\right) = \sum_{i=1}^{n} \arccos\left(\frac{\mathbf{s}_i^{con} : \mathbf{s}_i^{cp}}{\|\mathbf{s}_i^{con}\| \, \|\mathbf{s}_i^{cp}\|}\right)\frac{1}{n} \tag{6.1}$$

The reason the deviatoric stress is used to calculate the error is to avoid a hydrostatic pressure effect. If the hydrostatic pressure is large, the angle between two stress points will be very small, and in the limit of infinite pressure, zero. However, if the deviatoric stress is used, there will be no such effect, and the error measure will be sound for all hydrostatic pressures. Likely this is not a big issue, as the combination of elasticity and the boundary conditions used for the experiments, prevent very large pressures. However, since it is a straightforward correction to perform, there is no apparent reason not to use the deviatoric stress.

For the optimization scheme, the error is treated as a function of the model parameters, $c_1$, $c_2$, $c_3$ and $\theta_{crit}$. The optimization algorithm used is a gradient descent method, using a backtracking line-search algorithm. The Armijo-Goldstein condition is used to find an acceptable step length, as given in chapter six of the book "Numerical Methods for Unconstrained Optimization and Nonlinear Equations" by Dennis and Schnabel [9].

$$\mathbf{x} = \begin{bmatrix} c_1 \\ c_2 \\ c_3 \\ \theta_{crit} \end{bmatrix} \tag{6.2}$$

$$\boldsymbol{\nabla} f = \begin{bmatrix} \frac{\partial f}{\partial x_1} \\ \frac{\partial f}{\partial x_2} \\ \frac{\partial f}{\partial x_3} \\ \frac{\partial f}{\partial x_4} \end{bmatrix} \tag{6.3}$$

$$\mathbf{p} = -\frac{\boldsymbol{\nabla} f}{\|\boldsymbol{\nabla} f\|} \tag{6.4}$$

$$\mathbf{x}_{n+1} = \mathbf{x}_n + \alpha \mathbf{p} \tag{6.5}$$

$$f\left(\mathbf{x}_{n+1}\right) < f\left(\mathbf{x}_n\right) + \alpha\beta \mathbf{p}^{\mathrm{T}} \boldsymbol{\nabla} f \tag{6.6}$$

The acceptance criterion for the line-search is given by equation 6.6. $\delta$ is the step length, with initial value $\delta = 0.5$. $\beta$ is a parameter determining how strict the criterion is. If $\beta = 1$, the algorithm demands that the decrease is greater than that predicted by the linearization of the function. However, due to curvature, this criterion will cause the algorithm to take too short steps, as the step size must be very small for the criteria to be fulfilled. If for instance, $f$ has positive curvature, it is even possible that such a solution is never found. A common initial guess is $\beta = 0.5$, which was proposed by Armijo [2] in the original paper presenting the method. If the criterion is not fulfilled, the step-length, $\delta$, is reduced by a factor $\frac{1}{2}$, and the criterion is checked again. This is performed until a satisfactory step length is determined.

The parameters are not free to take any value, and consequently, restrictions must be made to ensure that a step does not produce an invalid solution. If the solution is inside the solution domain, and the step oversteps the boundary, the step length is reduced such that the new solution lies at the boundary. However, if the original solution is already a boundary solution and the component of $\mathbf{p}$ in this direction sends the solution out of the domain, the component of $\mathbf{p}$ in this direction is set to zero, forcing the solution to move along the boundary, rather than over it. Since the limitations on the parameters are independent constants, at least in the non-hardening case, this simple scheme should be appropriate to ensure that a valid solution is found. The constraints for the different parameters are given in equations 6.7. The limitations for $c_1$ and $c_2$ are calculated from the condition that $\alpha$, in the constitutive model, must be positive.

$$\begin{aligned} 0 < c_1 &< \frac{1 - \frac{\langle h \rangle}{G}}{\sqrt{\frac{g}{G}}} \\ 0 < c_2 &< \frac{G}{\langle h \rangle}\left(1 - \sqrt{\frac{g}{G}}\right) \\ 0 < c_3 &< 1 \\ 0 < \theta_{crit} &< \frac{\pi}{2} \end{aligned} \tag{6.7}$$

# 7 Results and Discussion

Since the model proposed by Yoshida in 2018 [36] is the most recent, it is the one which will be investigated in this study. Both Yoshidas 2017 model and the one proposed by Kuroda and Tvergaard appear to be viable options and the author believes the simple and intuitive form of the Kuroda and Tvergaard model makes it unwise to rule it out.

As elaborated in detail in section 5, two types of boundary conditions have been implemented. In stress control, the stress direction is specified, usually in the $\sigma_{11} - \sigma_{22}$ plane. In strain control $D_{11}$ and $D_{22}$ are prescribed, and all stress components, except $\sigma_{11}$ and $\sigma_{22}$, are required to be zero. Since experiments in stress control result in the two models reaching the yield surface at the same spot, strain path change experiments have been performed by an initial deformation using stress control, followed by an abrupt change of strain path, in strain control. Hence all strain path change experiments performed are of this type.

The results presented in this study are for a non-hardening material, as hardening brings further complexity to an already quite complex comparison. However the framework for doing experiments on a hardening material is fully implemented both for the crystal plasticity model and the constitutive model and if such simulations are of interest it is relatively straight forward to perform using the code available online [13].

## 7.1 The $\Theta$-$\Theta_p$ relation

In order to test how the model behaves just after a strain path change, Yoshida has investigated the relation between $\theta^p$ and $\theta$ at the moment of the the strain path change. This relation illustrates to what extent $\mathbf{D}^p$ is allowed to tilt at the instant of the strain path change. The experiment is interesting both to investigate the behaviour of the crystal plasticity simulations and to see if the implemented model produces the same results as the ones provided by Yoshida [34] [36], which it should.

The angles are calculated according to equation 7.1 and 7.2. $\bar{\mathbf{D}}^p_L$ is $\mathbf{D}^p$ from the last

time-step before the strain path change and $\bar{\mathbf{D}}^p_{NL}$ is the $\mathbf{D}^p$ from the first time-step after the strain path change. In the implementation of the model used in this study the last time-step before the strain path change has high precision due to the algorithm used to find the correct strain. $\bar{\mathbf{D}}^p_{NL}$ is taken as $\mathbf{D}^p$ from the first time-step after the strain path change, and if the time-step is reduced before making the strain path change, this gives the instant value. It should be noted that since the model follow the associated flow rule closely for linear loading paths, $\bar{\mathbf{D}}^p_L \approx \mathbf{N}$, which makes $\Theta$ a good approximation of $\theta$, which is the angle determining the inclination of $\mathbf{D}^p$ in the constitutive model.

$$\Theta^p = \frac{\bar{\mathbf{D}}^p_L : \bar{\mathbf{D}}^p_{NL}}{\left\|\bar{\mathbf{D}}^p_L\right\| \left\|\bar{\mathbf{D}}^p_{NL}\right\|} \tag{7.1}$$

$$\Theta = \frac{\bar{\mathbf{D}}^p_L : \mathbf{D}'}{\left\|\bar{\mathbf{D}}^p_L\right\| \|\mathbf{D}'\|} \tag{7.2}$$

The relation between $\Theta^p$ and $\Theta$ has been computed from both the crystal plasticity model and the constitutive model. The results are given in figure 7.1. If the produced results are compared with the figures presented by Yoshida in 2018 [36], it is evident that the implemented constitutive model produces the same results. For the crystal plasticity simulations the results seem to be roughly the same as the ones presented by Yoshida. However, there is some variation depending on the initial stress direction and the specific strain path change. The blue lines in figure 7.1 are for experiments performed with initial deformation in the stress direction $\sigma_{22} = -\sigma_{11}$ and the red lines are for an initial deformation in the $\sigma_{22} = \sigma_{11}$ direction. The author believes the correlation between the results for the constitutive model indicates that the implemented model produces the same results as the one implemented by Yoshida.

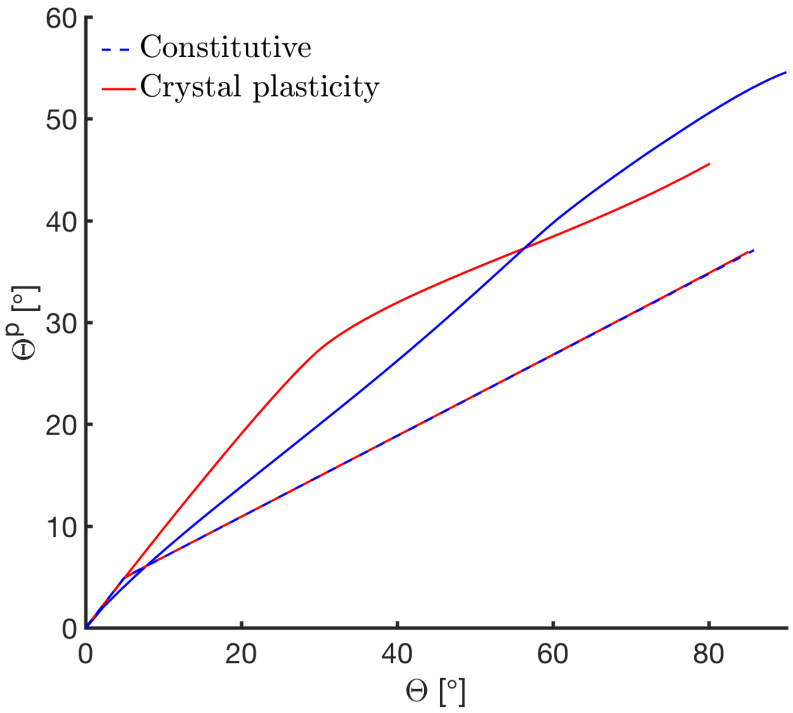


**Figure 7.1:** Relation between $\Theta^p$ and $\Theta$. The relation for the constitutive model is given by the overlapping dashed lines. The $\Theta^p - \Theta$ relation from the crystal plasticity model is given by the full lines. Blue lines indicate that the strain path change is from tensile-compression and the red lines from equibiaxial tension.

## 7.2 Strain path change experiments

To compare the constitutive model to the crystal plasticity model, several strain path change experiments have been performed . Equibiaxial load has been pointed out as the loading mode where the formation of a vertex on the yield surface is of importance [22]. Biaxial loads are also the loading modes for which the formation of a yield surface vertex is essential for predicting realistic limit strains for onset of necking [32] [28]. Therefore the virtual experiments in this study have been performed in this loading mode, followed by an abrupt strain path change into plane strain defomration mode.

The first order comparison between the constiutive and crystal plasticity model has been performed qualitatively for some abrupt change of strain paths by comparing stress paths,

the direction of $\mathbf{D}^p$ and the angles between $\mathbf{D}^p$ and $\mathbf{N}$ and between $\mathbf{D}^p$ and $\mathbf{D}$. To maintain simplicity, the preliminary comparison have been performed on a non hardening material. The model parameters initially provided by Yoshida have been used and are listed in table 7.1

**Table 7.1:** Model parameters proposed by Yoshida

| Parameter | $c_1$ | $c_2$ | $c_3$ | $\theta_{crit}$ [°] |
|---|---|---|---|---|
| Value | 0.3 | 0.5 | 0.4 | 5° |

In the virtual experiments presented in this subsection, the material is first deformed in equibiaxial stress control to an equivalent strain of $\bar{\epsilon}^p = 0.02$. The boundary condition is then abruptly changed to strain control with $D_{11} = 1$ and $D_{22} = 0$, corresponding to plane strain tension. The new strain path is kept until a total plastic strain of $\bar{\epsilon}^p = 0.04$ is reached.

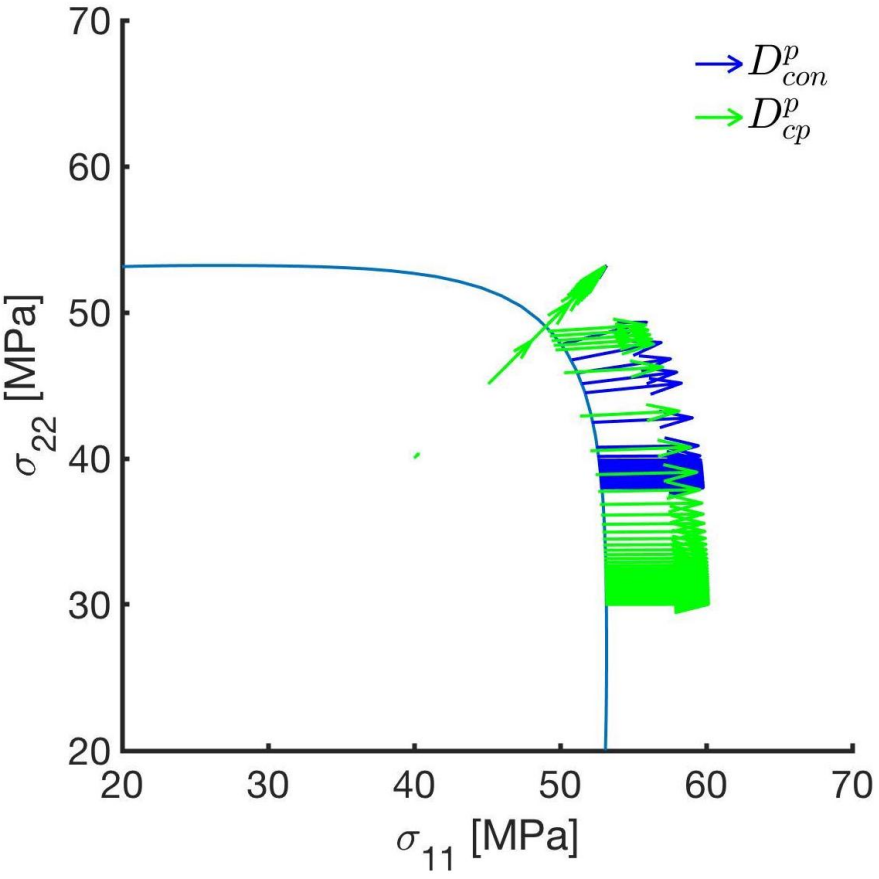


**Figure 7.2:** Arrows indicating $\mathbf{D}^p$ in its corresponding stress point. Hence the trace of the arrow tails show the stress path. Points have been selected at specific equivalent strains, the same for both models. $\mathbf{D}^p$ from the crystal plasticity model is given in green, and $\mathbf{D}^p$ from the constitutive model in blue.

As is evident from the plot in figure 7.2 the constitutive model initially slides faster along the yield surface than the crystal plasticity model. The constitutive model then comes almost to a stop, and moves at a rate much slower than the crystal plasticity model. This is also evident from the angle between $\mathbf{D}^p$ and $\mathbf{N}$, as it decreases very slowly towards zero when the model has passed into the region where $\theta$ is below $\theta_{crit}$. Since $\mathbf{D}^p$ is close to parallel with $\mathbf{D}$, the angle between $\mathbf{D}^p$ and $\mathbf{N}$ should be approximately equal to $\theta$. Consequently it can be seen that the model changes regime, when the angle between $\mathbf{D}^p$ and $\mathbf{N}$ of the constitutive model falls below $\theta_{crit}$, which is 5°.

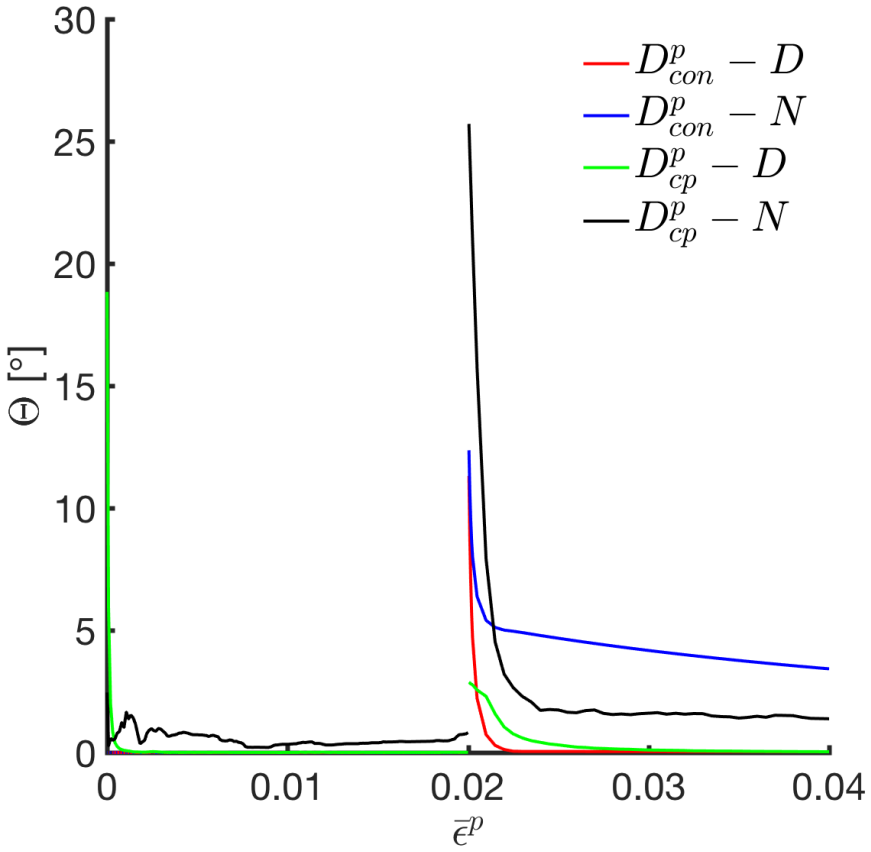


**Figure 7.3:** Plot of the angle between $\mathbf{D}^p$ and $\mathbf{N}$ and $\mathbf{D}^p$ and $\mathbf{D}$ for the two models.

The results presented above clearly indicate that the model, with the parameters provided by Yoshida [36], does not greatly mimic the behaviour observed from the crystal plasticity model. It does however incorporate the corner effect, and creates a transition from one strain or stress path to another, so qualitatively it does what it is supposed to. If however it is the case that the model fits the simulations and experiments performed by Yoshida very accurately, it might indicate that there are large variations in the loading modes investigated. Therefore simulations in other loading modes, like for instance shear-tension, would be of interest. It may however seem reasonable to conclude that even though the models both incorporate the corner effect the rate at which the models slide along the yield surface is quite different.

A fundamental difference between the two models is that the crystal plasticity model is able to slide inside the yield surface, something the constitutive model can not. Con-

sequently if one assumes that the energy barrier between biaxial load and plane strain is the quantity governing the onset of necking, it is possible that the constitutive model needs to slide at a different pace than the crystal plasticity model in order to compensate for the shortcut through the yield surface.

## 7.3 Erratic relation between $\mathbf{D}^p$ and $\mathbf{N}$

There has been observed some noise in the computed angle between $\mathbf{D}^p$ and $\mathbf{N}$ from the crystal plasticity model. The phenomenon is present in figure 7.3, and even more pronounced in figure 7.6 in the next section. The cause of this erratic behavior is of interest, as it is desirable to know if it is related to numerical noise or is intrinsic to the model. Hence some investigation has been done.

The erratic behavior or noise of the angle between $\mathbf{D}^p$ and $\mathbf{N}$ is believed to be caused by the shear components of $\mathbf{D}^p$. In principle, there should be no shear components of $\mathbf{D}^p$, if the material was completely isotropic, but due to numerical inaccuracies and possibly a not fully isotropic set of grains, some small shear components are introduced in the iterative scheme to find a solution fulfilling the boundary conditions. To verify this hypothesis, a simulation has been performed, where the angle between the normal and only the diagonal part of $\mathbf{D}^p$ is used, instead of $\mathbf{D}^p$ with its shear components. The result is a much smoother relation between $\mathbf{D}^p$ and $\mathbf{N}$, as is shown in figure 7.4.

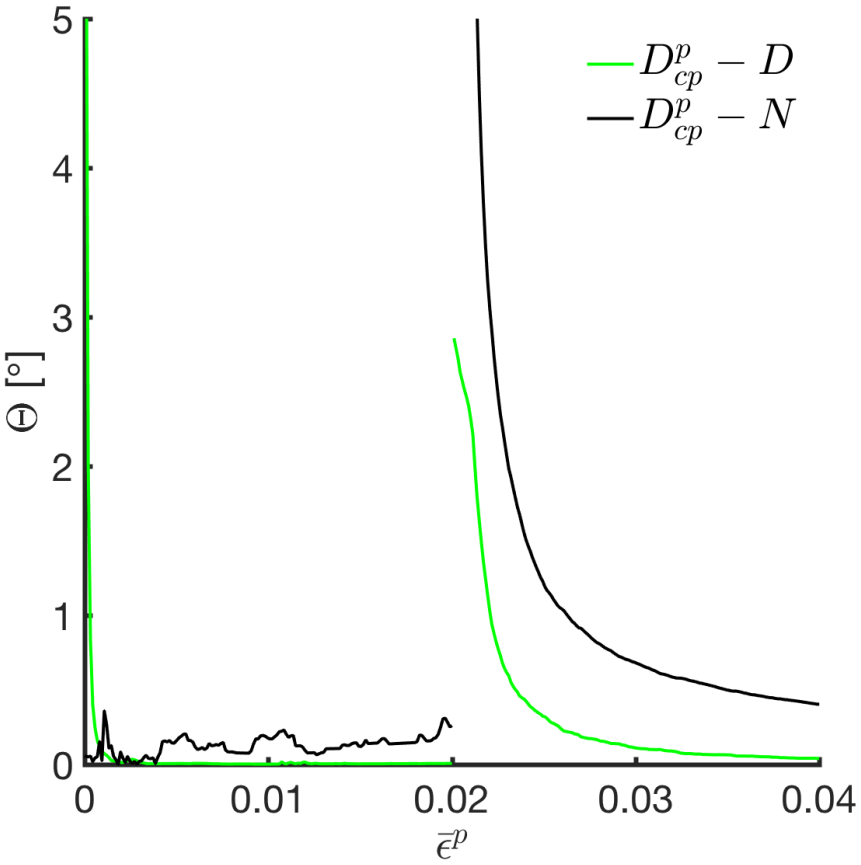


**Figure 7.4:** The angle between the diagonal of $\mathbf{D}^p$ and $\mathbf{N}$, for a strain path change from $\sigma_{22} = \sigma_{11}$ to $D_{11} = 1$ and $D_{22} = 0$.

Before the strain path change, the angle between $\mathbf{D}^p$ and $\mathbf{N}$ is still slightly erratic. This is likely due to numerical noise and dependent on the specific stress path. The stress path is $\sigma_{11} = \sigma_{22}$, which is a direction where a perturbation in deformation or stress rate will cause large variations in the normal, as it is the region of the yield surface with the most curvature. Consequently, to test this hypothesis a strain path change in the opposite direction has been performed, with initial stress direction $\sigma_{22} = \frac{1}{2}\sigma_{22}$ and a strain path change into $D_{11} = D_{22}$, corresponding to equibiaxial tension. As can be seen from the plot in figure 7.5 the behavior, in this case, is very close to associated, however there are still some variations. It makes sense that numerical inaccuracies have less impact when the initial load is onto the straighter part of the yield surface, where a minor change in for instance stress, will produce a very small perturbation of the yield surface normal.

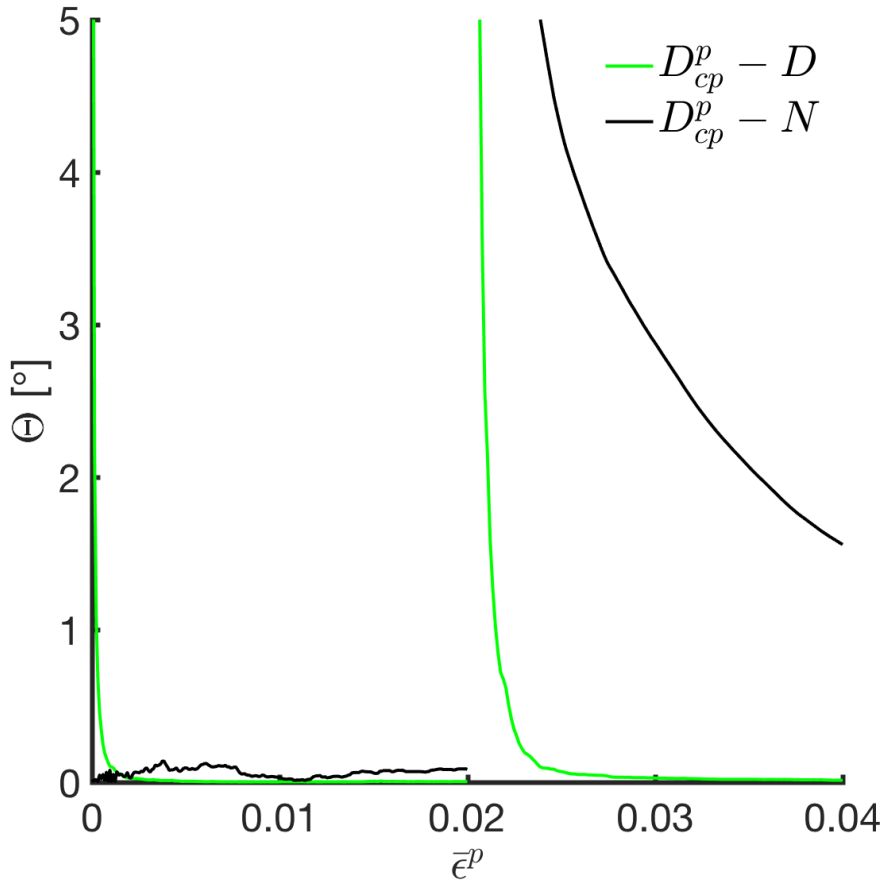


**Figure 7.5:** The angle between the diagonal of $\mathbf{D}^p$ and $\mathbf{N}$, for a strain path change from $\sigma_{22} = \frac{1}{2}\sigma_{11}$ to $D_{11} = D_{22}$.

## 7.4 Associated flow

From the virtual strain path change experiments, it may seem like the crystal plasticity model does not reach associated flow. Since the angle between $\mathbf{D}^p$ and $\mathbf{N}$ does not saturate at zero, as is clear from the plot of the angle between the two tensors given in figure 7.3. If the $\mathbf{D}^p$ and $\mathbf{N}$ had been coaxial the flow would have been associated, as the plastic strain increment would be parallel to the normal of the yield surface, which is the case for the associated flow rule. The explanation for this behavior has not been completely determined, however, some suggestions are made.

It is not obvious to the author that the crystal plasticity model must be associated,

and consequently, it might happen that a stationary solution is found before the model reaches associated flow. This is supported by the fact that the angle between $\mathbf{D}^p$ and $\mathbf{D}$ rapidly drops to zero. As is explained in section 2.5, coaxiality between $\mathbf{D}$ and $\mathbf{D}^p$ implies that there is no $\mathbf{D}^e$ and hence the stress point is stationary. This argument is naturally also valid for the crystal plasticity model. If $\mathbf{D}$ and $\mathbf{D}^p$ reach coaxiality before reaching associated flow, the loading point will stop sliding along the surface and consequently never reach the point corresponding to the associated flow.

In order to test this hypothesis a strain path change experiment was performed, as described in the preceding section, the only difference being that at the end, an additional strain path change was made, tilting $\mathbf{D}$ a degree upwards the $\sigma_{11} - \sigma_{22}$ plane. Hence the initial stress direction is $\sigma_{11} = \sigma_{22}$ to a von Mises plastic strain of $\bar{\epsilon}^p = 0.02$, followed by strain control with $D_{11} = 1$ and $D_{22} = 0$ up to $\bar{\epsilon}^p = 0.04$, as in the experiment in figure 7.3. Further the strain path was changed to $D_{11} = \cos\left(\frac{\pi}{180}\right)$ and $D_{22} = \sin\left(\frac{\pi}{180}\right)$, which is a reverse change of one degree. If the stress point remains the same, there is likely something to the hyopthesis that associated flow is never reached. The result is given in figure 7.6.

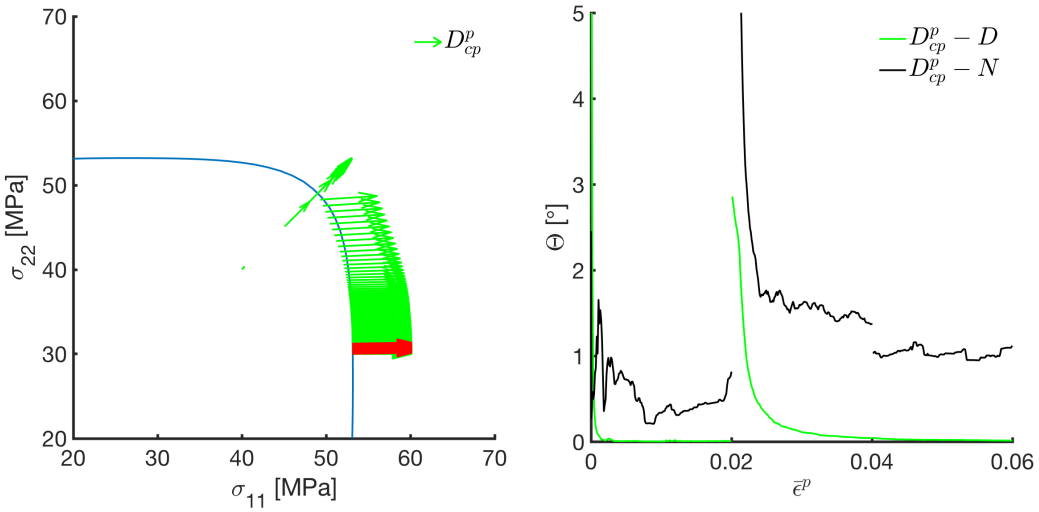


**Figure 7.6:** The results from the simulation attempting to determine if the crystal plasticity model does not reach associated flow, but stops at an earlier stage. A third strain path change is performed tilting $\mathbf{D}$ one degree upwards.

Several such strain path changes between 0.25° and 5° upward reversals have been performed, all yielding similar results, with the angle saturating at roughly 1°. Consequently, this is not the hysteresis effect believed to be the reason for the non-associated behavior.

In the preceding section, the shear components of $\mathbf{D}^p$ was removed, and the resulting angle with $\mathbf{N}$ removed most of the erratic variation of the angle otherwise observed. The shear components may also be the actual explanation why the crystal plasticity model does not seem to reach associated flow. To test this hypothesis, a simulation to higher strains have been performed calculating the angle between $\mathbf{D}^p$ without shear components, and $\mathbf{N}$. As is apparent from the plot in figure 7.7, the angle between the diagonal of $\mathbf{D}^p$ and $\mathbf{N}$ saturates at about 0.25° which is such a small value that there is little reason to believe the model does not saturate to associated flow. The deviation might now be explained by poor yield surface fitting, numerical noise or possibly texture development. Oppositely, an alteration to the actual $\mathbf{D}^p$ is needed to acquire this result, and in order to be entirely certain that the model saturates to associated flow, further investigations should be made, for instance using an even larger set of grains than the 936 grains used for the simulations in this study, to be completely certain that the aggregate used give isotropic behavior.

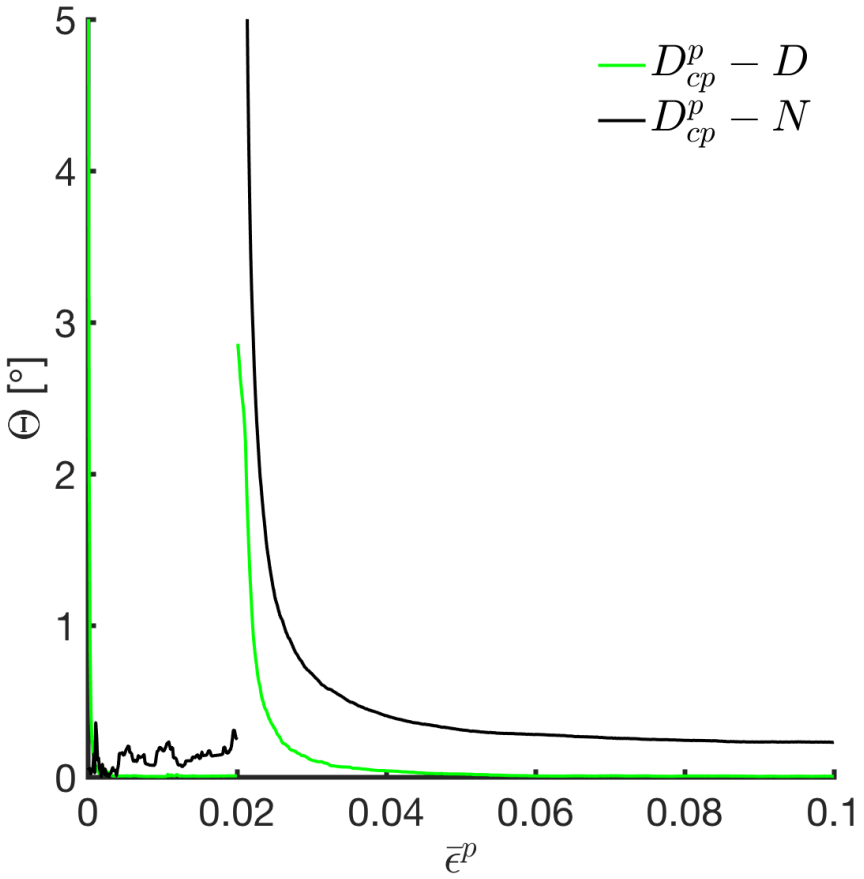


**Figure 7.7:** The angle between the diagonal of $\mathbf{D}^p$ versus $\mathbf{N}$ up to a strain of $\bar{\epsilon}^p = 0.1$, following a strain path change from equibiaxial tension to plane strain.

The constitutive model is inherently drawn towards associated flow, and at large strains following a strain path change, associated flow will be reached. This might not be the impression from the plots in section 7.2, as the model tends slowly towards associated flow with the model parameters provided by Yoshida. However, the model moves closer to the point where $\mathbf{D}'$ and $\mathbf{N}$ are coaxial. When coaxiality is achieved there is no longer a tangential component of $\mathbf{D}'$ and consequently the model degenerates to the associated flow rule. This behavior is more clear from the strain path changes performed using the fitted model parameters, shown in subsection 7.6.

## 7.5 The $\alpha - \theta$ relation

In the flow rule proposed by Yoshdia [34], $\alpha$ determines the fraction of the tangential component of $\mathbf{D}'$ that goes into $\mathbf{D}^p$. Hence it controls how much $\mathbf{D}^p$ is tilted. Due to the additive decomposition of $\mathbf{D}$ into an elastic and a plastic part, this in turn determines the magnitude of $\mathbf{D}^e$, at least for a non-hardening material, for which the only permissible direction of the stress rate is tangential to the yield surface, as the yield surface does not expand. A similar argument is made by Simo [31], who points out that for a non hardening material, $\mathbf{D}^e$, and hence the stressrate, is zero if $\mathbf{D}^p$ is coaxial with $\mathbf{D}$. Consequently, $\alpha$ determines the speed at which the stress slides along the yield surface. The crystal plasticity behaviour of $\alpha$ is therefore of great interest. Both to determine if the form of the proposed model is well suited, and to find good initial guesses for the model parameters.

$$\mathbf{D}^p = \dot{\lambda}\mathbf{N} + \alpha \mathbf{D'}_t \tag{7.3}$$

The flow rule used in the constitutive model is as given in equation 7.3. If it is assumed that the crystal plasticity model follow the Hoshford yield surface, $\alpha$ may be computed from the stresspoint, $\mathbf{D}$, and $\mathbf{D}^p$. As proposed in equation 36 by Yoshida [34], the tangential component of the deviatoric deformation rate may be found according to equation 7.4.

$$\begin{aligned} \mathbf{D'}_t &= \mathbf{T} : \mathbf{D} \\ \mathbf{T} &= \mathbf{I}^{4s} - \frac{1}{3}\mathbf{I} \otimes \mathbf{I} - \mathbf{n} \otimes \mathbf{n} \\ I^{4s}_{ijkl} &= \frac{1}{2}\left(\delta_{ik}\delta_{jl} + \delta_{il}\delta_{jk}\right) \end{aligned} \tag{7.4}$$

By the same procedure, a projection operator, $\mathbf{P}$, projecting onto $\mathbf{D'}_t$ may be defined according to equation 7.5.

$$\mathbf{P} = \frac{\mathbf{D'}_t}{\|\mathbf{D'}_t\|} \otimes \frac{\mathbf{D'}_t}{\|\mathbf{D'}_t\|} \tag{7.5}$$

$$\mathbf{D}_t^p = \mathbf{P} : \mathbf{D}^p \tag{7.6}$$

Finally the component of $\mathbf{D}^p$ along the direction $\mathbf{D'}_t$ is found according to equation 7.6. $\alpha$ is then computed as the relative length of the tangential components of $\mathbf{D}^p$ and $\mathbf{D'}$, according to equation 7.7.

$$\alpha = \frac{\|\mathbf{D}_t^p\|}{\|\mathbf{D'}_t\|} \tag{7.7}$$

The assumption that the crystal plasticity model follows the Hoshford yield surface is at least qualitatively reasonable. The yield surface normal is solely dependent on the stress direction, and hence, two stresspoints along the same radial direction will have the same gradient. If the plot of the stress paths from strain path change experiments are studied, it is clear that the crystal plasticity model shortcuts through the internal of the yield surface. However the stress direction does not seem to change substantially, and qualitatively it is reasonable to use the Hoshford yield surface. This is also the one used in the constitutive model, which further supports the assumption.

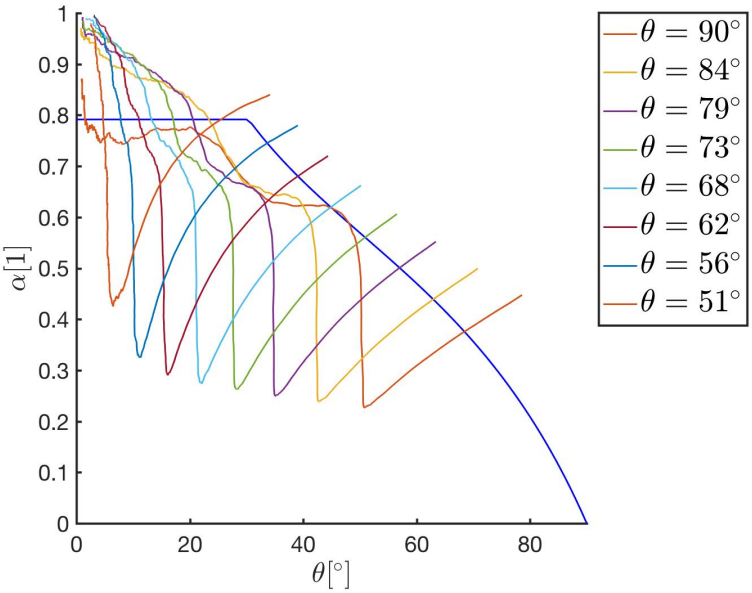


**Figure 7.8:** The development of $\alpha$ as a function of $\theta$, the angle between $\mathbf{D}'$ and $\mathbf{N}$. The blue line with a kink, is $\alpha$ from the constitutive model using the parameters found using the optimization algorithm.

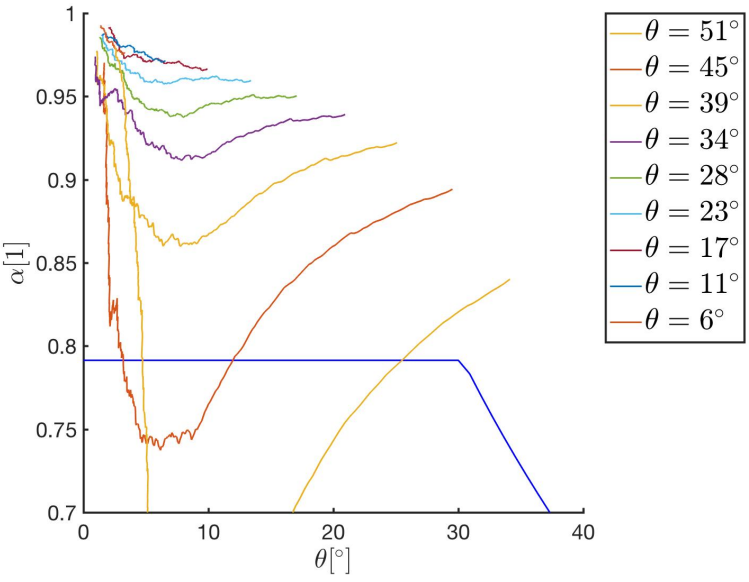


**Figure 7.9:** The development of $\alpha$ as a function of $\theta$, the angle between $\mathbf{D}'$ and $\mathbf{N}$. The blue line with a kink is $\alpha$ from the constitutive model using the parameters found using the optimization algorithm.

The behaviour of $\alpha$ is computed from a set of strain path change experiments. 16 strain path changes with $\theta$ between 0° and 90° have been performed from equibiaxial tension, meaning that the stress direction is $\sigma_{11} = \sigma_{22}$ during the initial deformation. 16 experiments have also been simulated in the opposite direction, from compression-tension meaning that $\sigma_{22} = -\sigma_{11}$ during the initial deformation. The observed behaviour of $\alpha$ for the equibiaxial experiments are given in figures 7.8 and 7.9. Results from the strain path changes from tensile-compression experiments is given in figures 7.10 and 7.11.

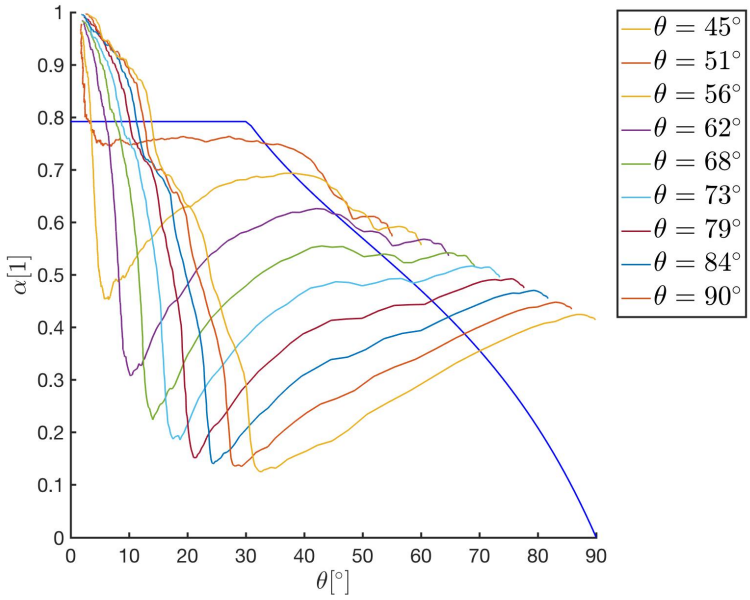


**Figure 7.10:** The development of $\alpha$ as a function of $\theta$, the angle between $\mathbf{D}'$ and $\mathbf{N}$, from strain path change experiments deviation from strain-compression initial deformation. The blue plotted line is $\alpha$ from the constitutive model using the parameters found using the optimization algorithm.

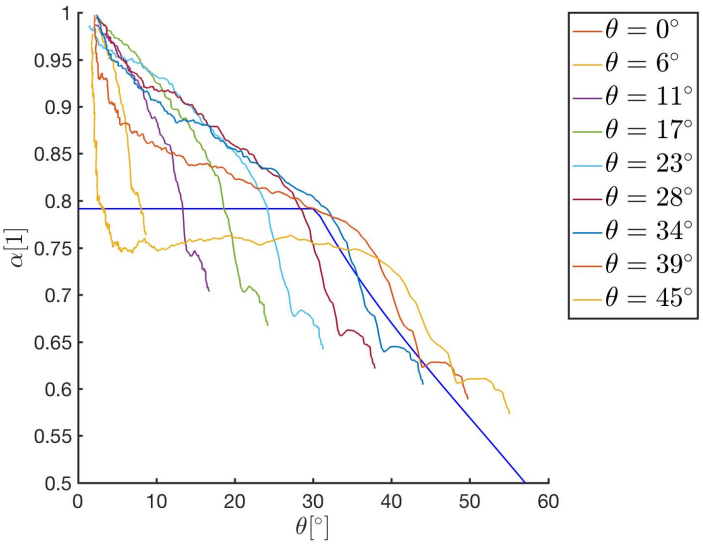


**Figure 7.11:** The development of $\alpha$ as a function of $\theta$, the angle between $\mathbf{D}'$ and $\mathbf{N}$, from strain path change experiments deviation from strain-compression initial deformation. The blue plotted line is $\alpha$ from the constitutive model using the parameters found using the optimization algorithm.

From the plot of $\alpha$ in figures 7.8, 7.9, 7.10 and 7.11 , it is quite clear that the inherent $\alpha - \theta$ relation of the crystal plasticity is not static and only a function of $\theta$ as the one implemented in the proposed flow rule. It seems like the relationship varies depending on the initial tilt angle of the strain path change, hence using a definition of $\alpha$ only dependent on the current $\theta$ may not be suitable. If the behavior should be described, it seems like $\alpha$ seeks towards the straight line from 1 at zero degrees to 0 at 90°, however with some over-swing. Hence it is possible that some sort of differential equation may be more suitable to determine $\alpha$. At low angles, plotted in figure 7.9 and 7.11, the behaviour is similar, and $\alpha$ takes a slight dip before rising fast towards 1 when $\theta$ falls below $\approx 7° - 8°$.

The behavior from the experiments in equibiaxial stress and the experiments in tensile-compression show some of the similar behavior, but there are slight differences. The experiments in tensile-compression, seem to better accommodate the larger strain path changes as the calculated $\theta$ reach about the same value as what is prescribed in the strain path change. This is not the case for the experiments from equibiaxial stress, as

the computed angle from these experiments seems to be substantially lower than the prescribed strain path change. A possible explanation for this behavior is the curvature of the yield surface, which is much larger in the corner of equibiaxial load, than along the almost straight line of the tensile-compression point. Hence when only a small timestep has been made the yield surface normal will tilt faster in a region of high curvature, and likewise, tilt very slowly in regions of less curvature. This trend is somewhat present as the decrease, or change in $\alpha$ is larger for the equibiaxial case than in for the tensile-compression experiment, which starts from a straight part of the yield surface.

The reason for the almost linear decrease and sharp change in $\alpha$ seen for the larger strain path changes is not understood. It is unclear which mechanism is causing $\alpha$ to initially decrease, before it rises towards unity. This behavior is observed in both cases, however not as pronounced in the tensile-compression case as in the equibiaxial case, which is believed to be related to the local curvature of the yield surface.

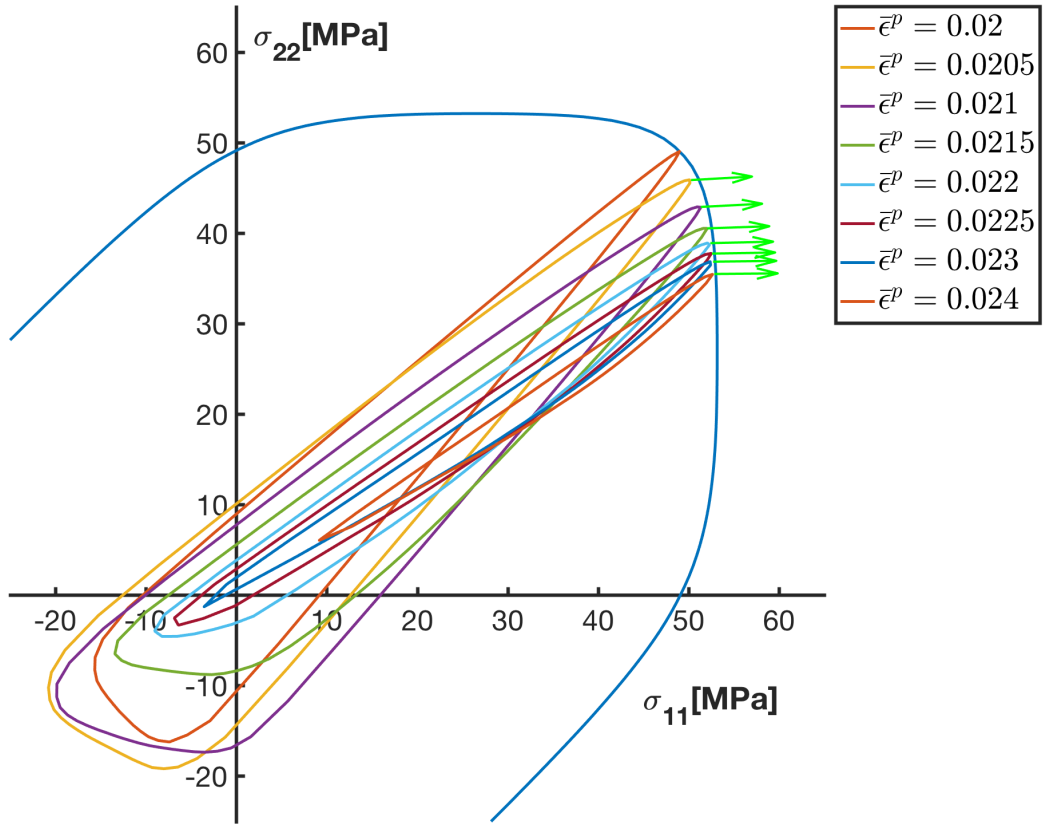


**Figure 7.12:** Plot of development of instantaneous yield surfaces for increasing offset strain. It appears that the instantaneous yield surface becomes increasingly narrow with increasing strain after the strain path change. The offset strain for the yield surfaces is $\bar{\epsilon} = 0.0000002$.

One possible explanation is that $\mathbf{D}^p$ is able to tilt quite much in the beginning due to the vertex on the instantaneous yield surface. To investigate if the behavior may be related to the vertex angle, a set of instantaneous yield surfaces have been calculated for a strain path change from equibiaxial tension to plane strain. These are presented in figure 7.12. It appears that the angle remains quite sharp, despite the surfaces being calculated at an offset strain of $\bar{\epsilon} = 0.0000002$. The overall trend seems to be that the instantaneous yield surfaces become narrower, and computing such narrow instantaneous yield surfaces is difficult since the material must be unloaded without entering the plastic region. It

seems like $\mathbf{D}^p$ stays inside the vertex throughout the experiment. Otherwise, there is no apparent explanation between the behavior of $\alpha$ and the instantaneous yield surface. The instantaneous yield surfaces are also of interest on its own, and the development of these could be an interesting topic for further work.

## 7.6 Optimization of flow rule parameters

It has been attempted to fit the model parameters of the flow rule to the values giving the smallest distance in deviatoric stress between points of equal strain. However as have been revealed in the previous section, section 7.5, where the $\alpha - \theta$ relation is studied, it might be impossible to fit a model which is optimum in all cases. Since the behavior is largely dependent on the magnitude of the initial strain path change. The ideal parameters should likely be chosen by optimizing many different strain path change experiments simultaneously, to find a set of parameters which fits most experiments in an acceptable way. However due to the findings of the $\alpha - \theta$ relation this has not been done, as the optimization algorithm is quite slow, especially if many stress points must to be used. The method may still be useful for calibration of the model, as the proposed method of model calibration, proposed by Yoshida [34], is through the elastoplastic tangent modulus, which is computationally complex to acquire.

**Table 7.2:** Table listing fitted model parameters

| Parameter | $c_1$ | $c_2$ | $c_3$ | $\theta_{crit}$ [1] |
|---|---|---|---|---|
| Value | 6.92795 | 0.5 | 0.5213 | 0.53007 |

The model parameters have been fitted for the experiment where the strain path is changed from equibiaxial tension to plane strain, that is from $\sigma_{11} = \sigma_{22}$ in stress control over to strain control with $D_{11} = 1$ and $D_{22} = 0$. The reason this is the strain path change that is investigated, is that for necking to take place, the deformation rates in the material must locally reach a state of plane strain, hence the transition is of interest for instability prediction [32]. However, as the optimization revealed, the strain path change might

have been too small, as the critcal vertex angle $\theta_{crit}$, and consequently $c_3$, is fully ruled out. Meaning that the found optimum angle is larger than the maximum $\theta$ throughout the experiment. The fitted parameters are listed in table 7.2. The experimental fit between the constitutive model and the crystal plasticity model improved greatly, both quantitatively, and qualitatively, as is shown in figure 7.13.

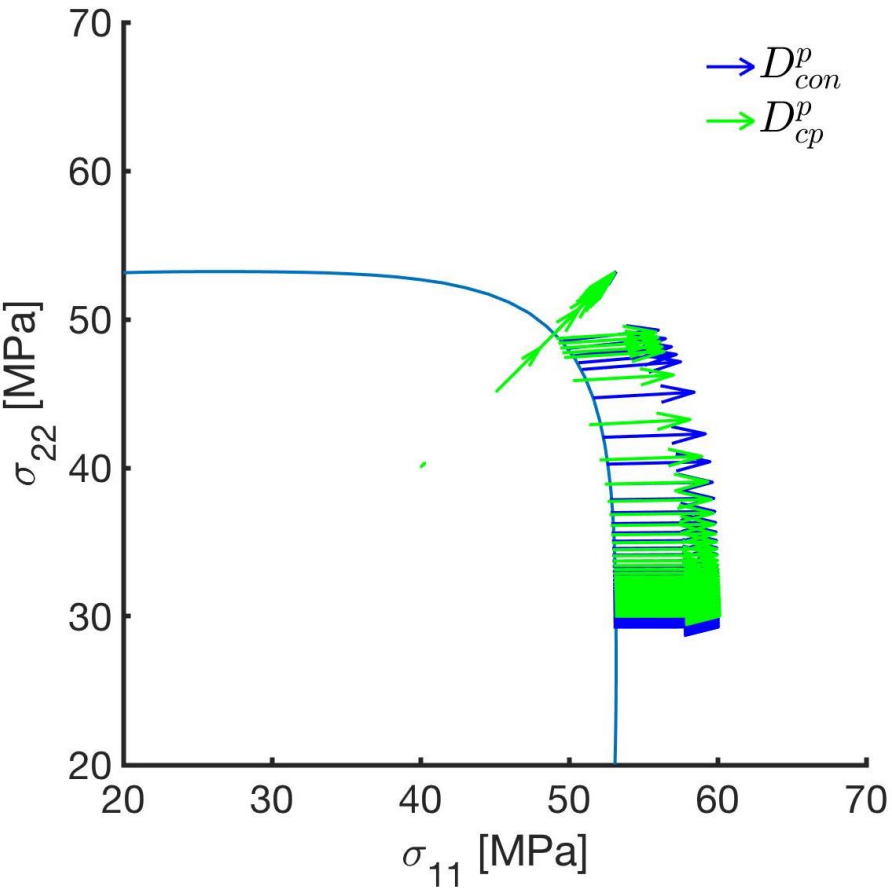


**Figure 7.13:** Illustration of the stress path and $\mathbf{D}^p$ for a strain path change from equibiaxial load to plane strain, using the fitted model parameters.

It is evident from the illustration if the strain path change experiment using the fitted parameters that a better fit is obtained. An interesting trend is that the constitutive model slides faster in the beginning, then slower and in the end faster than the crystal plasticity model. This behaviour is supported by the computed $\alpha - \theta$ relation shown in figure 7.14, where it is clear that $\alpha$ from the crystal plasticity model is higher than for

the constitutive model for large $\theta$. It is then lower from roughly $12° - 13°$ down to $\approx 4°$ before it rises rapidly towards 1. Since $\alpha$ controls the tilt of $\mathbf{D}^p$, a lower value implies greater sliding speed along the yield surface. Consequently the observed behaviour of the stress path and $\mathbf{D}^p$ and the computed values of $\alpha$ is in accordance with each other.

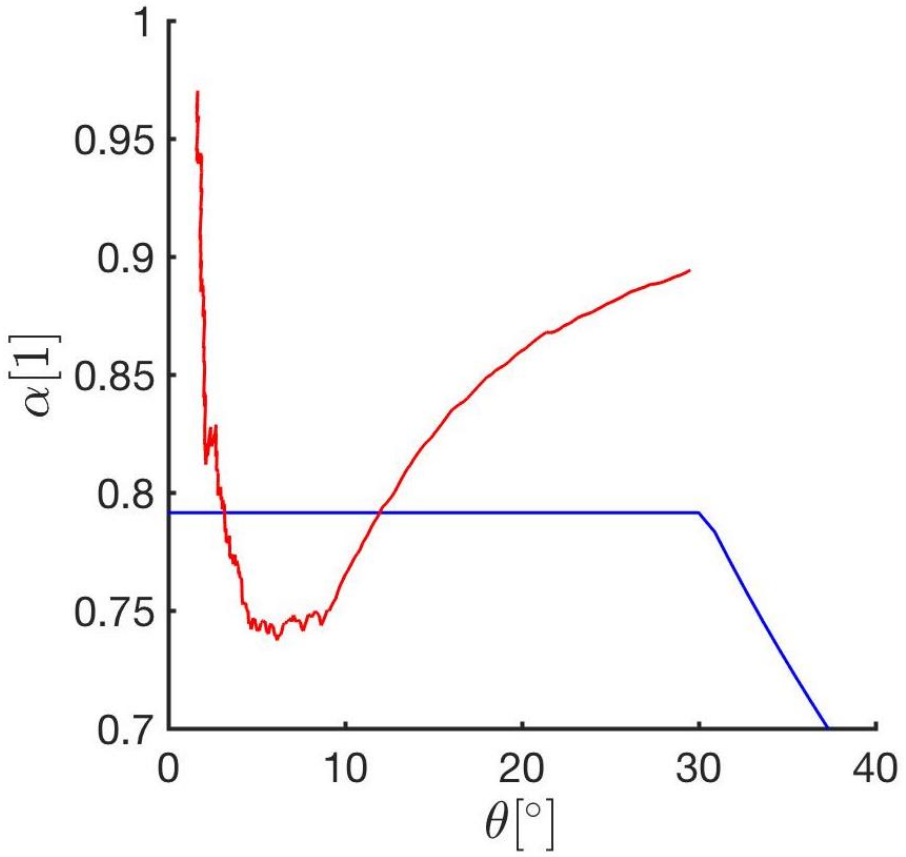


**Figure 7.14:** The relation between $\alpha$ from the constitutive model, using fitted parameters, and the crystal plasticity model.

## 7.7 Non energy conjugated strain meassure

The use of the von Mises equivalent plastic strain in all of the proposed non-associated flow theories seems odd to the author, as it would be more natural to use a work conjugate strain measure. The von Mises equivalent strain is the work conjugate of von Mises equivalent stress. Hence, if a different yield surface is used, and consequently a different equivalent stress, the natural would be to select the corresponding conjugate

strain measure.

The consequence of this choice of strain measure is that the yield surface will no longer correspond to a given plastic work, but the plastic work will vary along the surface. To investigate this behavior a yield surface has been calculated from the constitutive model for a constant plastic work, to investigate if there are significant deviations between the surface at a given offset strain and at a given plastic work. The plastic work is computed according to equation 7.8 and the results of the simulations are given in figure 7.15.

$$\begin{aligned} \dot{W}^p &= \boldsymbol{\sigma} : \mathbf{D}^p \\ W^p &= \int_0^t \dot{W}^p dt \end{aligned} \tag{7.8}$$

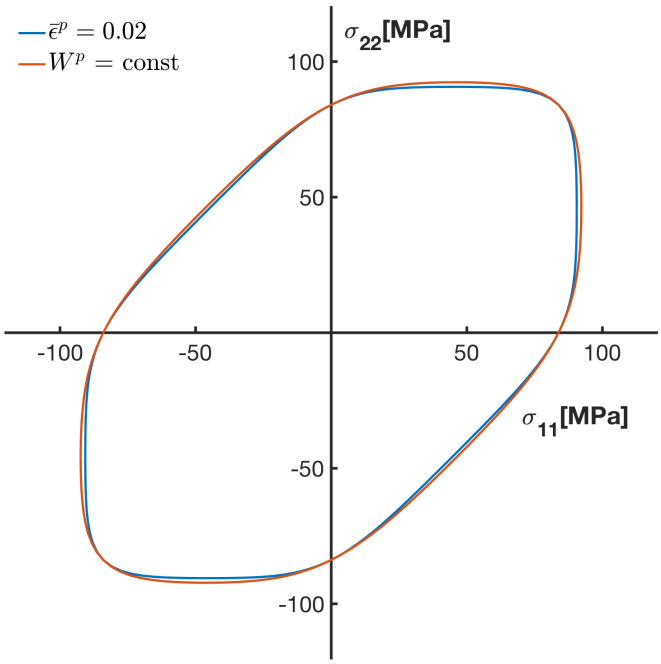


**Figure 7.15:** Yield surface at offset strain of $\bar{\epsilon}^p = 0.02$ and at constant plastic work. The surface was calcultated to the plastic work found for a uniaxial tensile test to $\bar{\epsilon}^p = 0.02$, and cosequently the two meassures match at this location.

There can clearly be seen a slight deviation between the yield surface at constant work

and the one at a constant equivalent strain. The difference is however not very large, and the strain measure is likely acceptable to use. However, the notion that the yield surface corresponds to a given plastic work is not correct in this case. It is the author's belief that using the von Mises strain is something that is left from the original model proposed by Simo, who uses the von Mises yield surface. Since there is not presented any argument why an energy-conjugate strain measure is not used, in any of the later models. Consequently, introducing an energy-conjugate strain measure would make the model more in line with conventions. Although, there might be reasons not to do so, the only reason apparent to the author being that the von Mises strain is explicitly given, easing calculations.

## 7.8 Dissipation of plastic energy

Plastic deformation is an irreversible process, and consequently for a phenomenological plasticity model to be thermodynamically sound, production of plastic energy is not permitted. It is relatively simple to prove for the von Mises yield surface that the plastic energy dissipates. Since the yield surface normal is always radial in the $\pi$-plane, any $\mathbf{D}^p$ at an angle less or equal to $\pi/2$ will have possitive dissipation of energy. However, it is not equally apparent when different yield surfaces are used. Consequently, it remains to be proven that the more general models, like the one from Yoshida [34], does not permits dissipation of plastic energy. The workaround is to verify that the plastic work is positive for each timestep.

# 8 Conclusions

The constitutive model, incorporating a corner effect, proposed by Yoshida [36] has been implemented. A new reverse map integration algorithm for the model havs been developed, which better ensures consistency throughout the experiments than the explicit method originally proposed by Yoshida [34].

In parallel the elastoplastic rate-independent Taylor-Lin crystal plasticity model has been implemented and verified to be used in comparison and to calibrate the phenomenological plasticity model.

A framework for performing virtual experiments has been built for both the models, which makes it possible to perform simulations of virtual experiments in both stress and strain control, while staying within given boundary conditions.

The two models have been qualitatively compared by performing strain path change experiments and comparing stress paths, direction of plastic deformation gradients and the angles between the plastic deformation gradient, the yield surface normal and the total deformation gradient. The results reveal that both models qualitatively incorporate a corner effect, as the plastic deformation rate is allowed to tilt instantly, and the loading point moves quite rapidly along the yield surface. On the contrary, the two models seem to slide along the surface at relatively different speeds, at least when using the original model parameters provided by Yoshida.

The parameter $\alpha$ as a function of tilt angle, $\theta$, was computed from the crystal plasticity model, revealing that the formulation for $\alpha$ from the constitutive model seems to be inherently unsuited to generally fit all types of strain path changes, at least in the $\sigma_{11}-\sigma_{22}$ plane for which the investigations have been conducted.

Prior to the investigation of $\alpha$, an optimization algortihm was implemeted in order to fit the model parameters such as to minimize the average distance between stresspoints in deviatoric stress space from the two models. This is done for a given experiment, and is regarded as a quantitative meassure of the deviation between the models. The

results gave much better agreement between the sliding speed along the yield surface for the experiment which was fitted. As pointed out, it seems difficult to fit the model parameters, so that they suit all kinds of strain path changes, but an adequate fit may be found for some specific cases.

The overall conclusion is that the model qualitatively incorporates the corner effects, but the fit between the crystal plasticity model and the constitutive model is not quite satisfactory in a qualitative perspective, at least not for all experiments. The fact that the earlier proposed way of calibrating the constitutive model involves computation of the elastoplastic tangent modulus, which is an intricate calculation, and the fact that four fitting parameters are needed, might speak in favour of the simpler model proposed by Kuroda and Tvergaard [21]. It is clear that the Kuroda and Tvergaard model will also incorporate the corner effect, but the model is simpler and uses only two model parameters, $c$ and $\theta_{crit}$. Consequently, it might be hard to justify computing the elastoplastic tangent modulus, otherwise surplus in an implicit formulation, and all four parameters for a model that is not in a better agreement with the crystal plasticity model. Implementing the Kuroda and Tvergaard model for comparison would therefore be of interest.

Further work on the subject of non-associated flow rules should in the authors opinion maybe not focus on developing more new models, but on supporting the ones already present, such that the models are adapted. The models all degenerate to the associated flow rule for proportional loading paths, and hence is consequently an expansion of the associated flow rule. The reasons why these models are not adapted should be investigated, and the issues resolved, before novel models are developed. On the contrary, the results reveal that new, more advanced models, might also be in line, if the behavior of the crystal plasticity model is to be reproduced precisely.

# References


[1] L. Anand and M. Kothari. «A computational procedure for rate-independent crystal plasticity». eng. In: *Journal of the Mechanics and Physics of Solids* 44.4 (1996), pp. 525–558.

[2] L Armijo. «Minimization of functions having Lipschitz continuous first partial derivatives». eng. In: *Pacific Journal of Mathematics* 16.1 (1966), pp. 1–3.

[3] Morris Azrin and Walter Backofen. «The deformation and failure of a biaxially stretched sheet». eng. In: *Metallurgical Transactions* 1.10 (1970), pp. 2857–2865.

[4] F. Barlat. «Crystallographic texture, anisotropic yield surfaces and forming limits of sheet metals». In: *Materials Science and Engineering* 91 (1987), pp. 55–72.

[5] Frédéric Barlat, Daniel J. Lege, and John C. Brem. «A six-component yield function for anisotropic materials». eng. In: *International Journal of Plasticity* 7.7 (1991), pp. 693–712.

[6] S B Batdorf and Bernard Budiansky. *A mathematical theory of plasticity based on the concept of slip*. eng. 1949.

[7] Ted Belytschko. *Nonlinear Finite Elements for Continua and Structures*. eng. Second edition. John Wiley & Sons Ltd, 2013.

[8] J. Christoffersen and J.W. Hutchinson. «A class of phenomenological corner theories of plasticity». eng. In: *Journal of the Mechanics and Physics of Solids* 27.5 (1979), pp. 465–487.

[9] J. Dennis and R. Schnabel. *Numerical Methods for Unconstrained Optimization and Nonlinear Equations*. Society for Industrial and Applied Mathematics, 1996.

[10] George E Dieter. *Mechanical metallurgy*. eng. London, 1988.

[11] S. Dumoulin, O.S. Hopperstad, and T. Berstad. «Investigation of integration algorithms for rate-dependent crystal plasticity using explicit finite element codes». eng. In: *Computational Materials Science* 46.4 (2009), pp. 785–799.

[12] O. Engler and V. Randle. *Introduction to Texture Analysis: Macrotexture, Microtexture, and Orientation Mapping, Second Edition*. CRC Press, 2009.

[13] Bjørnar Gjesdal. *Github Repository*. 2019. URL: `https://github.com/bjorgjes/iypoint/releases/tag/1.0` (visited on 06/07/2019).

[14] S.S. Hecker. In: *Experimental Studies of Yield Phenomena in Biaxially Loaded Metals, in Constitutive Equations in Viscoplasticity: Computational and Engineering Aspects* (1976). cited By 3, pp. 1–33.

[15] R. Hill. «On discontinuous plastic states, with special reference to localized necking in thin sheets». In: *Journal of the Mechanics and Physics of Solids* 1.1 (1952), pp. 19–30.

[16] R. Hill. «The essential structure of constitutive laws for metal composites and polycrystals». In: *Journal of the Mechanics and Physics of Solids* 15.2 (1967), pp. 79–95.

[17] W. F. Hosford. «A Generalized Isotropic Yield Criterion». eng. In: *Journal of Applied Mechanics* 39.2 (1972).

[18] S.R. Kalidindi, C.A. Bronkhorst, and L. Anand. «Crystallographic texture evolution in bulk deformation processing of FCC metals». eng. In: *Journal of the Mechanics and Physics of Solids* 40.3 (1992), pp. 537–569.

[19] Akhtar S Khan. *Continuum theory of plasticity*. eng. New York ; Chichester, 1995.

[20] Erwin Kreyszig, Herbert Kreyszig, and E. J. Norminton. *Advanced Engineering Mathematics*. Tenth. Hoboken, NJ: Wiley, 2011.

[21] Mitsutoshi Kuroda and Viggo Tvergaard. «A phenomenological plasticity model with non-normality effects representing observations in crystal plasticity». eng. In: *Journal of the Mechanics and Physics of Solids* 49.6 (2001), pp. 1239–1263.

[22] Mitsutoshi Kuroda and Viggo Tvergaard. «Shear band development predicted by a non-normality theory of plasticity and comparison to crystal plasticity predictions». eng. In: *International Journal of Solids and Structures* 38.50 (2001), pp. 8945–8960.

[23] T. Kuwabara et al. «Use of abrupt strain path change for determining subsequent yield surface: experimental study with metal sheets». eng. In: *Acta Materialia* 48.9 (2000), pp. 2071–2079.

[24] T.H. Lin. «Analysis of elastic and plastic strains of a face-centred cubic crystal». eng. In: *Journal of the Mechanics and Physics of Solids* 5.2 (1957), pp. 143–149.

[25] T.H. Lin and M. Ito. «Theoretical plastic distortion of a polycrystalline aggregate under combined and reversed stresses». In: *Journal of the Mechanics and Physics of Solids* 13.2 (1965), pp. 103–115.

[26] Tomáš Mánik and Bjørn Holmedal. «Review of the Taylor ambiguity and the relationship between rate-independent and rate-dependent full-constraints Taylor models». eng. In: *International Journal of Plasticity* 55 (2014), pp. 152–181.

[27] Zdzislaw Marciniak and Kazimierz Kuczyński. «Limit strains in the processes of stretch-forming sheet metal». eng. In: *International Journal of Mechanical Sciences* 9.9 (1967), 609, IN1, 613–612, IN2, 620.

[28] A. Needleman and V. Tvergaard. «Necking of biaxially stretched elastic-plastic circular plates». In: *Journal of the Mechanics and Physics of Solids* 25.3 (1977), pp. 159–183.

[29] Jwo Pan and James R. Rice. «Rate sensitivity of plastic flow and implications for yield-surface vertices». In: *International Journal of Solids and Structures* 19.11 (1983), pp. 973–987.

[30] G. Sachs. «Plasticity problems in metals». In: *Transactions of the Faraday Society* 24 (1928), pp. 84–92.

[31] J.C. Simo. «A J 2-flow theory exhibiting a corner-like effect and suitable for large-scale computation». eng. In: *Computer Methods in Applied Mechanics and Engineering* 62.2 (1987), pp. 169–194.

[32] S. Stören and J.R. Rice. «Localized necking in thin sheets». In: *Journal of the Mechanics and Physics of Solids* 23.6 (1975), pp. 421–441.

[33] G.I. Taylor. «Plastic Strain in Metals». eng. In: *Journal of the Institute of Metals* 62 (1938), pp. 307–324.

[34] Kengo Yoshida. «A plastic flow rule representing corner effects predicted by rate-independent crystal plasticity». In: *International Journal of Solids and Structures* 120 (2017), pp. 213–225.

[35] Kengo Yoshida and Mitsutoshi Kuroda. «Comparison of bifurcation and imperfection analyses of localized necking in rate-independent polycrystalline sheets». eng. In: *International Journal of Solids and Structures* 49.15-16 (2012), pp. 2073–2084.

[36] Kengo Yoshida and Takuma Tsuchimoto. «Plastic flow of thin-walled tubes under nonlinear tension-torsion loading paths and an improved pseudo-corner model». eng. In: *International Journal of Plasticity* 104 (2018), pp. 214–229.

[37] K. Zhang et al. «Assessment of advanced Taylor models, the Taylor factor and yield-surface exponent for FCC metals». In: *International Journal of Plasticity* (2018).

# A Gradient of Hoshford yield surface

The six-component hoshford yield surface is given by Barlat [5] according to the following set of equations.

$$A = \sigma_{22} - \sigma_{33} \qquad B = \sigma_{33} - \sigma_{11} \qquad C = \sigma_{11} - \sigma_{22}$$
$$F = \sigma_{23} \qquad G = \sigma_{13} \qquad H = \sigma_{12}$$

$$I_2 = \frac{F^2 + G^2 + H^2}{3} + \frac{(A-C)^2 + (C-B)^2 + (B-A)^2}{54}$$

$$I_3 = \frac{(C-B)(A-C)(B-A)}{54} + FGH - \frac{(C-B)F^2 + (A-C)G^2 + (C-B)H^2}{6}$$

$$\Theta = \arccos\left(\frac{I_3}{I_2^{3/2}}\right)$$

$$\Phi = (3I_2)^{m/2}\left\{\left[2\cos\left(\frac{2\Theta+\pi}{6}\right)\right]^m + \left[2\cos\left(\frac{2\Theta-3\pi}{6}\right)\right]^m - \left[2\cos\left(\frac{2\Theta+5\pi}{6}\right)\right]^m\right\} = 2\bar{\sigma}^m$$

In order to find the gradient of the yield surface the partial derivatives of the equivalent stress must be determined with respect to each of the stress components. However it is not necessary to calculate the derivative six times. By application of the chain rule it is possible to determine an expression for the gradient dependent of the partial derivatives of A,B,C,F,G and H. These derivatives are stored in a matrix, where the partial derivative of each with respect to the six stress components are stored. Hence the partial derivatives of $I_3$, $I_2$, $\Theta$ and $\Phi$ can be largely reused, only changing out the partial derivatives of each of the "letter" functions with respect to the relevant stress component. The matrix is given below

$$\begin{array}{c|cccccc} & A & B & C & F & G & H \\ \hline \sigma_{11} & \frac{\partial A}{\partial \sigma_{11}} & \frac{\partial B}{\partial \sigma_{11}} & \frac{\partial C}{\partial \sigma_{11}} & \frac{\partial F}{\partial \sigma_{11}} & \frac{\partial G}{\partial \sigma_{11}} & \frac{\partial H}{\partial \sigma_{11}} \\ \sigma_{22} & \frac{\partial A}{\partial \sigma_{22}} & \frac{\partial B}{\partial \sigma_{22}} & \frac{\partial C}{\partial \sigma_{22}} & \frac{\partial F}{\partial \sigma_{22}} & \frac{\partial G}{\partial \sigma_{22}} & \frac{\partial H}{\partial \sigma_{22}} \\ \sigma_{33} & \frac{\partial A}{\partial \sigma_{33}} & \frac{\partial B}{\partial \sigma_{33}} & \frac{\partial C}{\partial \sigma_{33}} & \frac{\partial F}{\partial \sigma_{33}} & \frac{\partial G}{\partial \sigma_{33}} & \frac{\partial H}{\partial \sigma_{33}} \\ \sigma_{23} & \frac{\partial A}{\partial \sigma_{23}} & \frac{\partial B}{\partial \sigma_{23}} & \frac{\partial C}{\partial \sigma_{23}} & \frac{\partial F}{\partial \sigma_{23}} & \frac{\partial G}{\partial \sigma_{23}} & \frac{\partial H}{\partial \sigma_{23}} \\ \sigma_{13} & \frac{\partial A}{\partial \sigma_{13}} & \frac{\partial B}{\partial \sigma_{13}} & \frac{\partial C}{\partial \sigma_{13}} & \frac{\partial F}{\partial \sigma_{13}} & \frac{\partial G}{\partial \sigma_{13}} & \frac{\partial H}{\partial \sigma_{13}} \\ \sigma_{12} & \frac{\partial A}{\partial \sigma_{12}} & \frac{\partial B}{\partial \sigma_{12}} & \frac{\partial C}{\partial \sigma_{12}} & \frac{\partial F}{\partial \sigma_{12}} & \frac{\partial G}{\partial \sigma_{12}} & \frac{\partial H}{\partial \sigma_{12}} \end{array} = \begin{bmatrix} 0 & -1 & 1 & 0 & 0 & 0 \\ 1 & 0 & -1 & 0 & 0 & 0 \\ -1 & 1 & 0 & 0 & 0 & 0 \\ 0 & 0 & 0 & 1 & 0 & 0 \\ 0 & 0 & 0 & 0 & 1 & 0 \\ 0 & 0 & 0 & 0 & 0 & 1 \end{bmatrix} \tag{A.1}$$

It then remains to calculate the derivative of the equivalent stress with respect to each of the six stress components.

$$\frac{\partial \bar{\sigma}_{eq}}{\partial \sigma_{ij}} = \frac{\partial}{\partial \sigma_{ij}} \left( \left[ \frac{\Phi}{2} \right]^{1/m} \right) = \frac{1}{m} \left[ \frac{\Phi}{2} \right]^{1/m-1} \frac{1}{2} \frac{\partial \Phi}{\partial \sigma_{ij}}$$

$$\frac{\partial \Phi}{\partial \sigma_{ij}} =$$
$$\frac{\partial}{\partial \sigma_{ij}} \left( (3I_2)^{m/2} \right) * \left\{ \left[ 2\cos\left( \frac{2\Theta + \pi}{6} \right) \right]^m + \left[ 2\cos\left( \frac{2\Theta - 3\pi}{6} \right) \right]^m - \left[ 2\cos\left( \frac{2\Theta + 5\pi}{6} \right) \right]^m \right\}$$
$$+ (3I_2)^{m/2} * \frac{\partial}{\partial \sigma_{ij}} \left\{ \left[ 2\cos\left( \frac{2\Theta + \pi}{6} \right) \right]^m + \left[ 2\cos\left( \frac{2\Theta - 3\pi}{6} \right) \right]^m - \left[ 2\cos\left( \frac{2\Theta + 5\pi}{6} \right) \right]^m \right\}$$

$$\frac{\partial}{\partial \sigma_{ij}} \left( (3I_2)^{m/2} \right) = \frac{2}{m} (3I_2)^{m/2-1} * 3 \frac{\partial I_2}{\partial \sigma_{ij}}$$

$$\frac{\partial I_2}{\partial \sigma_{ij}} = \frac{2\left( F \frac{\partial F}{\partial \sigma ij} + G \frac{\partial G}{\partial \sigma ij} + H \frac{\partial H}{\partial \sigma ij} \right)}{3} +$$
$$\frac{2\left( (A-C)\left( \frac{\partial A}{\partial \sigma ij} - \frac{\partial C}{\partial \sigma ij} \right) + (C-B)\left( \frac{\partial C}{\partial \sigma ij} - \frac{\partial B}{\partial \sigma ij} \right) + (B-A)\left( \frac{\partial B}{\partial \sigma ij} - \frac{\partial A}{\partial \sigma ij} \right) \right)}{54}$$

$$\frac{\partial}{\partial\sigma_{ij}}\left\{\left[2\cos\left(\frac{2\Theta+\pi}{6}\right)\right]^m+\left[2\cos\left(\frac{2\Theta-3\pi}{6}\right)\right]^m-\left[2\cos\left(\frac{2\Theta+5\pi}{6}\right)\right]^m\right\}$$
$$=\left\{m\left[2\cos\left(\frac{2\Theta+\pi}{6}\right)\right]^{m-1}\left(-2\sin\left(\frac{2\Theta+\pi}{6}\right)\frac{2}{6}+\right.\right.$$
$$m\left[2\cos\left(\frac{2\Theta-3\pi}{6}\right)\right]^{m-1}\left(-2\sin\left(\frac{2\Theta-3\pi}{6}\right)\frac{2}{6}\right.$$
$$\left.\left.-m\left[2\cos\left(\frac{2\Theta+5\pi}{6}\right)\right]^{m-1}\left(-2\sin\left(\frac{2\Theta+5\pi}{6}\right)\frac{2}{6}\right\}\frac{\partial\Theta}{\partial\sigma_{ij}}\right.$$

$$\frac{\partial\Theta}{\partial\sigma_{ij}}=\frac{-1}{\sqrt{1-\left(\frac{I_3^2}{I_2^3}\right)}}\frac{\frac{\partial I_3}{\partial\sigma_{ij}}I_2^{\frac{3}{2}}-\frac{3}{2}I_2^{\frac{1}{2}}\frac{\partial I_2}{\partial\sigma_{ij}}I_3}{I_2^3}$$

$$\frac{\partial I_3}{\partial\sigma_{ij}}=\frac{1}{54}\left(\left(\frac{\partial C}{\partial\sigma_{ij}}-\frac{\partial B}{\partial\sigma_{ij}}\right)(A-C)(B-A)+\right.$$
$$(C-B)\left(\left(\frac{\partial A}{\partial\sigma_{ij}}-\frac{\partial C}{\partial\sigma_{ij}}\right)(B-A)+(A-C)\left(\frac{\partial B}{\partial\sigma_{ij}}-\frac{\partial A}{\partial\sigma_{ij}}\right)\right)\Big)+$$
$$\frac{\partial F}{\partial\sigma_{ij}}GH+F\left(\frac{\partial G}{\partial\sigma_{ij}}H+G\frac{\partial H}{\partial\sigma_{ij}}\right)$$
$$-\left(\frac{2F}{6}\frac{\partial F}{\partial\sigma_{ij}}(C-B)+\frac{F^2}{6}\left(\frac{\partial C}{\partial\sigma_{ij}}-\frac{\partial B}{\partial\sigma_{ij}}\right)\right)$$
$$-\left(\frac{2G}{6}\frac{\partial G}{\partial\sigma_{ij}}(A-C)+\frac{G^2}{6}\left(\frac{\partial A}{\partial\sigma_{ij}}-\frac{\partial C}{\partial\sigma_{ij}}\right)\right)$$
$$-\left(\frac{2H}{6}\frac{\partial H}{\partial\sigma_{ij}}(B-A)+\frac{H^2}{6}\left(\frac{\partial B}{\partial\sigma_{ij}}-\frac{\partial A}{\partial\sigma_{ij}}\right)\right)$$

The gradient is then calculated by substituting the values of $A$, $B$, $C$, $F$, $G$ and $H$ and their respective partial derivatives with respect to each of the stress components and the gradient of the yield surface may be acquired.